

RESEARCH ARTICLE

10.1029/2018JC013785

Special Section:

Sea State and Boundary Layer
Physics of the Emerging Arctic
Ocean

Key Points:

- Airborne scanning lidar provides directional wavenumber spectra of the rapidly evolving wave field in the MIZ
- Wave attenuation in thin pancake ice is predominately dissipative
- Wave growth rates in ice-forming conditions are slightly higher than previous measurements under unstable atmospheric boundary layers

Supporting Information:

- Supporting Information S1

Correspondence to:

P. Sutherland,
peter.sutherland@ifremer.fr

Citation:

Sutherland, P., Brozena, J., Rogers, W. E., Doble, M., & Wadhams, P. (2018). Airborne remote sensing of wave propagation in the marginal ice zone. *Journal of Geophysical Research: Oceans*, 123, 4132–4152. <https://doi.org/10.1029/2018JC013785>

Received 12 JAN 2018

Accepted 26 APR 2018

Accepted article online 3 MAY 2018

Published online 28 JUN 2018

Airborne Remote Sensing of Wave Propagation in the Marginal Ice Zone

Peter Sutherland¹ , John Brozena², W. Erick Rogers³ , Martin Doble⁴ , and Peter Wadhams⁵ 

¹Laboratoire d’Océanographie Physique et Spatiale (LOPS), IFREMER, Plouzané, France, ²Naval Research Laboratory, Marine Geosciences Division, Washington, DC, USA, ³Naval Research Laboratory, Stennis Space Center, MS, USA, ⁴Polar Scientific, Ltd Appin, UK, ⁵Department of Applied Mathematics and Theoretical Physics, University of Cambridge, Cambridge, UK

Abstract Airborne scanning lidar was used to measure the evolution of the surface wave field in the marginal ice zone (MIZ) during two separate wave events in the Beaufort Sea in October 2015. The lidar data consisted of a 2-D field of surface elevation with horizontal resolutions between 17 and 33 cm, over a swath approximately 150–220 m wide, centred on the ground track of the aircraft. Those data were used to compute directional wavenumber spectra of the surface wave field. Comparison with nearby collocated buoy data found the lidar and buoy measurements to be generally consistent. During the first event, waves traveling from open water into the ice were attenuated by the ice. The low spectral spreading and $k^{7/4}$ spectral dependence of the attenuation was consistent with dissipative models that treat sea ice as a highly viscous fluid floating on a less viscous ocean. Upper-ocean eddy viscosities calculated using that model were found to be significantly lower than those from previous work. The second event was in off-ice winds and cold temperatures, allowing measurement of the wave fetch relation in ice-forming conditions. The wave growth rate was found to be slightly higher than previous measurements under unstable atmospheric conditions without ice formation. Comparison with WAVEWATCH III model output highlighted the importance of accurate ice information and fine geographic computational resolution when making predictions near the ice edge. Finally, the very short scales over which the wave field was observed to evolve in the MIZ are discussed.

1. Introduction

Sea ice coverage in the Arctic Ocean has been reducing since the beginning of the satellite record (e.g., Stroeve et al., 2011, 2014). This change is implicitly associated with an increase in open water. When winds blow over the ocean, they create waves, and the energy that can be transferred to the waves increases with distance (Hasselmann et al., 1973). Thus the increasing open water in the Arctic basin is expected to result in more energetic wave conditions, and initial studies appear to support that (Thomson & Rogers, 2014). The potential feedbacks of this changing wave climate on the remaining sea ice are not well understood. Waves are known to break up sea ice over large areas (Asplin et al., 2012; Collins et al., 2015; Liu & Mollo-Christensen, 1988; Meylan et al., 2014), potentially changing ice melt rates (Steele, 1992), and they also affect ice formation (e.g., Doble et al., 2003; Wadhams et al., 1987). It is clear, then, that understanding the propagation of waves in an icy environment is an important question in the context of a changing Arctic.

Sea ice is a highly varied medium, and numerous mechanisms have been proposed to describe its interactions with the wave field. The bulk of the literature has focussed on the scattering mechanism, wherein wave energy is scattered by individual floes or floe boundaries (e.g., Kohout & Meylan, 2008; Squire, 2007; Squire et al., 1995). Viscous attenuation has also been proposed as a mechanism for wave attenuation (Liu et al., 1991; Weber, 1987), and more recent work has attempted to combine the two mechanisms (Kohout et al., 2014). A key difference between scattering and dissipative attenuation is the effect on the directional spreading of the wave field; scattering broadens the spectra, approaching isotropy deep within the ice, whereas dissipation does not. The real-world relative importance of the various attenuation mechanisms remains an open question. Even less well studied are the effects of partial ice cover and ice formation on wave generation (Masson & Leblond, 1989).

Recent observational and modeling work has attempted to address some of these questions. For example, regarding attenuation mechanisms, evidence suggests that deep inside the ice pack, wave attenuation is predominantly dissipative (Ardhuin et al., 2016), and that nearer to the ice edge both dissipation and scattering are important (Sutherland & Gascard, 2016). However, the parameter space, of wave, wind, and ice conditions, available to more thoroughly test the various hypotheses regarding wave-ice interactions remains quite limited. This is largely due to the enormous technical challenges associated with operating in an active, wavy, MIZ. Although the first measurements of waves in sea ice were taken in the 1960s (Robin, 1963), until very recently only a few datasets were available (e.g., Squire & Moore, 1980; Wadhams, 1973; Wadhams et al., 1988).

The majority of past wave-in-ice studies have been single point measurements using buoys. Wave buoys with internal accelerometers, tilt-sensors, or GPS receivers are typically placed on floes or on buoys floating between floes, and time-series of their motion is recorded (Doble & Wadhams, 2006; Wadhams et al., 1988). The data are then treated with some variation of the processing proposed by Longuet-Higgins et al. (1963) to extract energy spectra, directionality, and spreading functions. Buoys mounted on floes are limited by the response of the floes to the water motions, which can be complicated. Sub-surface Acoustic Doppler Current Profilers (ADCPs) have also been used to measure wave motions in ice, producing similar outputs (Hayes et al., 2007). All of these in situ point measurements are extremely costly to deploy, difficult to adapt to changing conditions, and do not provide broad spatial coverage. The first spatial measurements of waves in sea ice were likely those by Wadhams (1975), who used an airborne single-point profiling lidar to follow a swell system into the sea ice. However, such a system requires a priori knowledge of the wave propagation direction, and interpretation becomes difficult if the aircraft flight direction is not directly aligned with the wave direction or if waves from multiple directions are present. Satellite-borne Synthetic Aperture Radar (SAR) provides global coverage and has also been used to compute the wavelength and directionality of waves in ice (Liu et al., 1991; Lyzenga et al., 1985; Schulz-Stellenfleth & Lehner, 2002). Recent advances (Ardhuin et al., 2015, 2017) have shown that it is also possible to extract directional wavenumber energy spectra. However, significant uncertainties remain regarding directional bias, reducing their utility for discriminating between attenuation mechanisms.

In this work, airborne scanning lidar was used to rapidly provide robust directional wavenumber spectra over large areas of the MIZ. The method developed by (Sutherland & Gascard, 2016) has been expanded upon in order to study both wave development and wave attenuation in the MIZ. The measurements were taken as part of the Office of Naval Research, "Sea State and Boundary Layer Physics of the Emerging Arctic Ocean" Departmental Research Initiative, during October 2015. As part of that program, in situ measurements and modeling results were available for comparison.

This paper is organized as follows: Section 2 describes the measurements. Section 3 describes the data processing and spectral calculations. Section 4 presents the results, covering: a description of the observed spectral evolution, comparison with buoy measurements, attenuation mechanisms, fetch relations, comparison with a spectral wave model, and rapid changes in ice conditions. Section 5 provides concluding remarks.

2. Measurements

The primary data type used in this work was scanning lidar imagery of the sea/ice surface. A Riegler Q560 near-infrared scanning lidar was mounted in the laser well of a modified DHC-6 Twin Otter aircraft. The instrument has a pulse repetition rate of 240 KHz and the beam was scanned at 160 Hz in the cross-flight direction. With a typical flight altitude of 220 m for Flight 2 (16 October 2015) and 150 m for Flight 4 (23 October 2015), this produced swaths of data approximately 255 m and 173 m across, respectively. Both flights had optimal along-track point spacings of 33 cm, and the cross-track spacing was 24 cm (swath centre) to 30 cm (swath edge) for Flight 2, and 17 to 25 cm for Flight 4. The data were geo-referenced using an Applanix POS-AV-510 GPS-INS to the EGM-08 (vertical) and WGS-84 (horizontal) reference frames. Typical short period (a few minutes) positioning errors were 2 cm with longer period errors due to GPS and EGM-08 errors of a meter or more. Examples of the data are given in Figure 1. As expected, over open water the point density decreases more rapidly than optimal with distance from the centre of the swath due to specular reflections from the sea surface. This effect is less pronounced over ice because of the diffuse nature of backscatter from the ice.

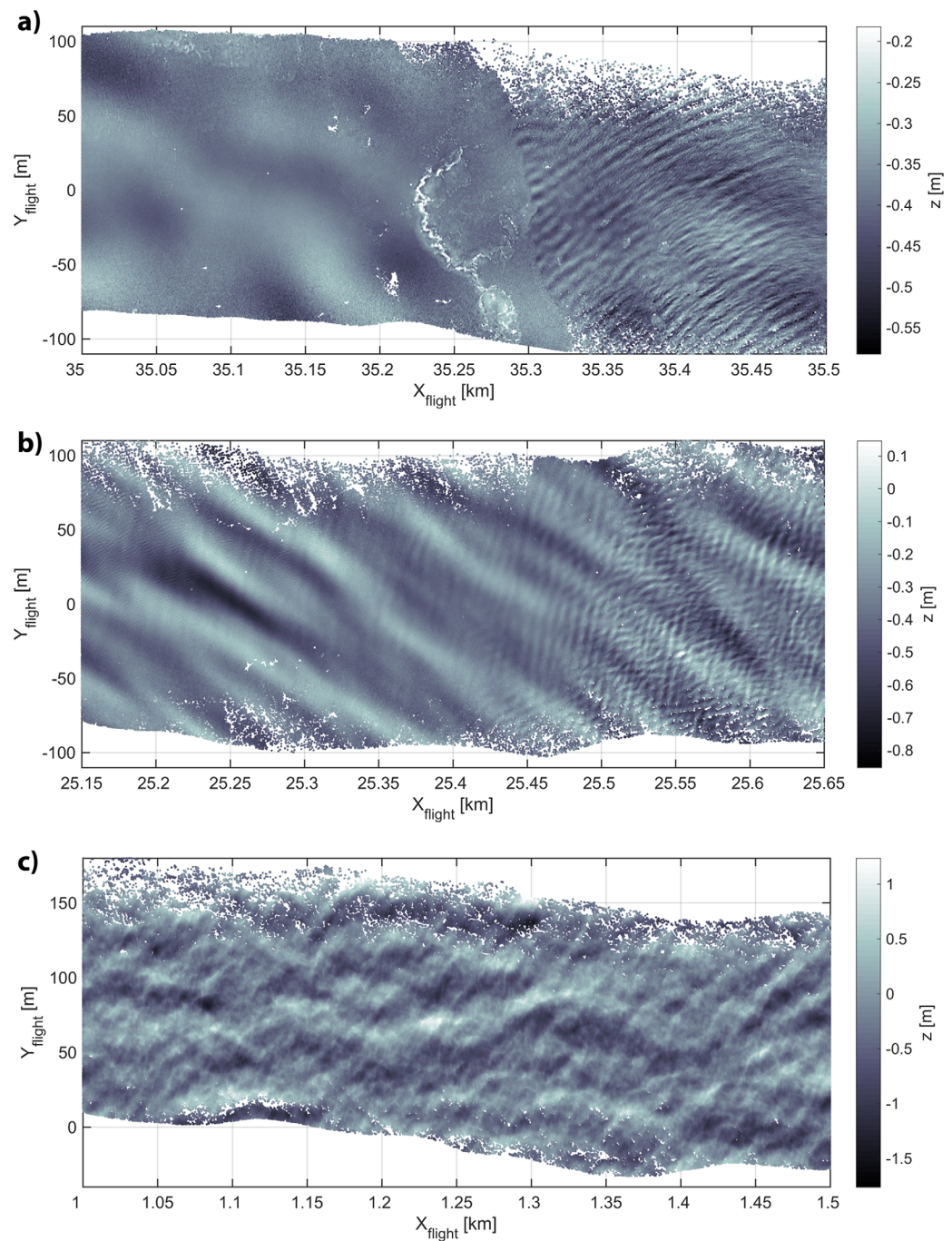


Figure 1. Examples of raw lidar images illustrating typical features of wave-ice interaction. Each gray-scale point corresponds to a single geo-referenced lidar return, and the colour corresponds to the elevation above the datum. All images are from a flight segment from Flight 4 (starting Oct. 23, 2015 at 21:32 UTC) during which the aircraft flew approximately 35 km from off-ice open-water towards and over the ice with a ground track of 32 deg. (meaning that the x-axis in these figures points towards 32 deg. true). The wind was approximately 11 m/s from 99 deg. true (coming from the lower right in these figures), and a swell from the SSE was also present. Panel a is deep within the ice, on the border of a lead and the ice. Panel b is farther toward open water, where the waves encounter a thin band of pancake ice. Panel c is the farthest away from the ice, in what is thought to be open water.

Of the total five flights during the experiment, two contained wave data usable for studying spectral evolution in sea ice, Flight 2, taken on 16 October 2015, and Flight 4, taken on 23 October 2015. Table 1 gives a summary of mean meteorological conditions during the flights, Figure 2 shows the large-scale ice cover

Table 1
Summary of Flights Analyzed and Their Associated Conditions

	Flight 2	Flight 4 (Wave array 6)
Date	16 October	23 October
Time (UTC)	21:16–22:09	20:54–22:58
Wind speed (m/s)	4.4	11
Wind dir. (deg.)	280	99
Temperature (C)	−2.6	−8.6

Note. Flight 4 corresponded to Wave Array 6 in Thomson et al. (2018). Meteorological measurements are from the met station aboard the R/V Sikuliaq and represent averages over the period starting 1 hour before the beginning of flight data acquisition and stopping 1 hour after the end of flight data acquisition. Wind direction is in degrees true in the “coming from” convention,

during the flights, and Figure 3 shows the modeled large-scale wave field (the model is discussed in section 4.5). During Flight 2, winds were approximately 4.4 m/s in the on-ice direction, from 280 deg. true, and the waves were directly in the on-ice direction. The flight path is shown in Figure 2, panels a and c, and consisted of a transect approximately paralleling the ice edge and extending up to approximately 15 km inside it. Flight 4 was somewhat more complicated; winds were approximately 11 m/s in the off-ice direction, from 99 deg. true. Waves were generated directly by the off-ice winds, but longer-period waves from the SSE was also present, generated by the same easterly wind system. The large-scale ice edge was oriented approximately north-west to south-east, oblique to the off-ice wind forcing and allowing the longer waves to form parallel to it (See supporting information for additional details). The flight path for Flight 4 is given in Figure 2, panels b and d; in that case, the aircraft flew several transects approximately orthogonal to the ice edge, as well as one that angled away at approximately 30 deg. from the edge.

3. Methods

The full wavenumber-frequency (k - ω) spectrum that describes the wave field, $\chi(\mathbf{k}, \omega)$, is defined such that

$$E = \langle \eta^2 \rangle = \iint \chi(\mathbf{k}, \omega) d\mathbf{k} d\omega. \quad (1)$$

where E is the wave energy, η is the surface elevation, \mathbf{k} is the wavenumber vector, and ω is the angular frequency (e.g., Phillips, 1977), that is related to the wavenumber by the dispersion relation. Significant wave height, H_s , is defined in terms of wave energy as

$$H_s \equiv 4E^{1/2}. \quad (2)$$

Direct measurement of $\chi(\mathbf{k}, \omega)$ requires spatio-temporal measurements of the sea surface which remain technically difficult to make, particularly over the range of scales typically present at the sea surface. Current efforts are largely focussed on stereo imaging (e.g., Benetazzo, 2006; Campbell et al., 2014) and X-band radar (e.g., Campana et al., 2017; Young et al., 1985), but both types of measurement have challenges regarding scale and/or interpretation. Instead it is more common to make measurements of projections of $\chi(\mathbf{k}, \omega)$.

The frequency spectrum can then be obtained by integrating $\chi(\mathbf{k}, \omega)$ over all wavenumbers,

$$\psi(\omega) = \int_{-\infty}^{\infty} \chi(\mathbf{k}, \omega) d\mathbf{k}, \quad (3)$$

and the directional frequency spectrum

$$\varphi(\omega, \theta) = \int_0^{\infty} \chi(k, \omega, \theta) k dk. \quad (4)$$

Here $k = |\mathbf{k}|$, and $\mathbf{k} = (k \cos \theta, k \sin \theta)$. The moments of the directional frequency spectra (Longuet-Higgins et al., 1963) are the most commonly measured projections of the full k - ω spectra. These are typically observed using wave buoys, both in open water (e.g., Herbers et al., 2012; Longuet-Higgins et al., 1963), and in sea ice (e.g., Doble & Bidlot, 2013; Wadhams et al., 1986).

In this work, the 2D wavenumber spectrum was measured. It is obtained by integrating $\chi(\mathbf{k}, \omega)$ over all frequencies,

$$F(\mathbf{k}) = \int_{-\infty}^{\infty} \chi(\mathbf{k}, \omega) d\omega. \quad (5)$$

The omnidirectional wavenumber spectrum is then defined as the integral of $F(\mathbf{k})$ over all angles,

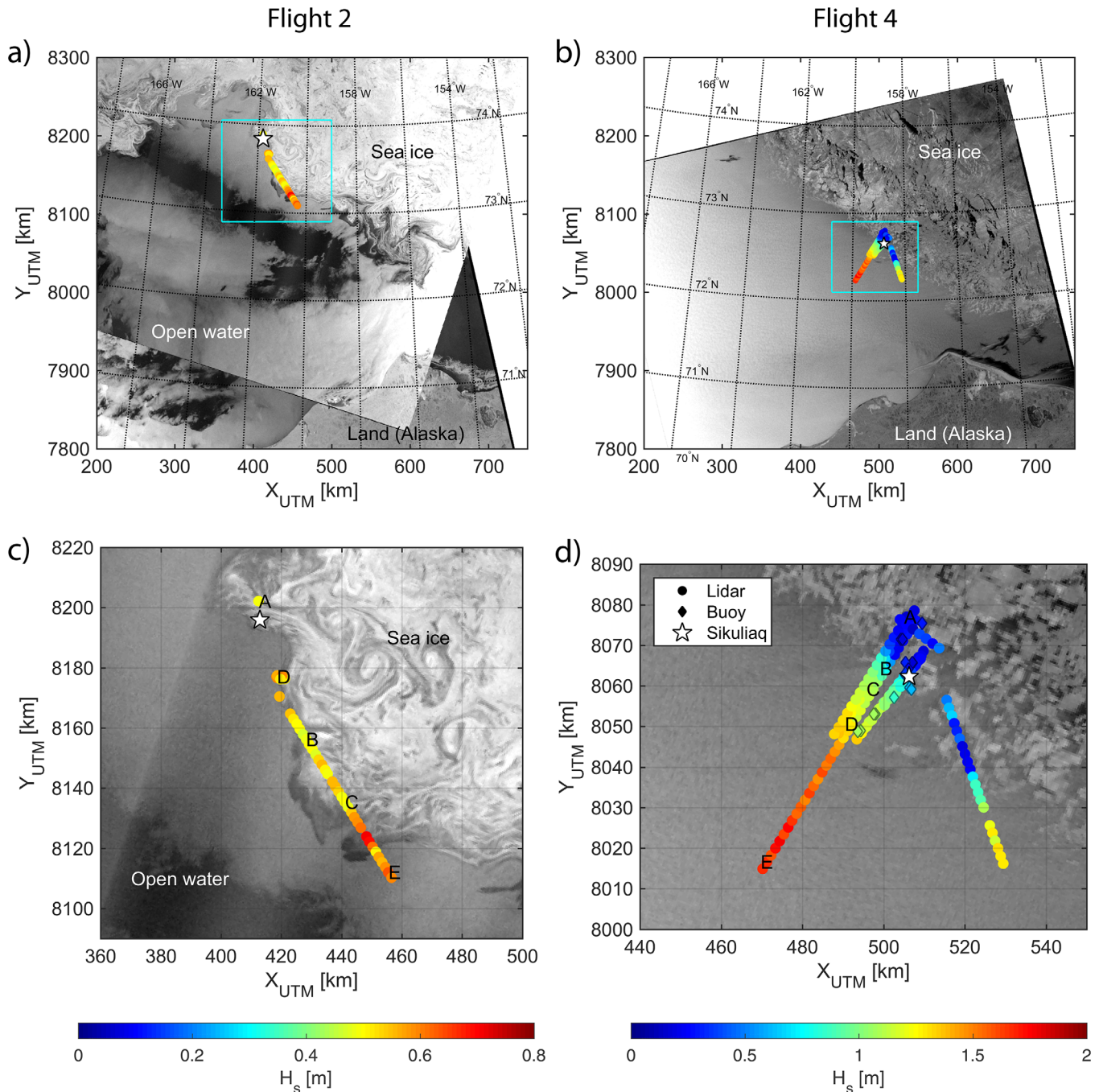


Figure 2. Maps of lidar flight paths relative to sea ice. In all panels, the background imagery is SAR backscatter from RADARSAT-2 (RADARSAT-2 Data and Products MacDonald, Dettwiler, and Associates Ltd., All Rights Reserved). The coloured circles show the flight path; each circle corresponds to a 2 km flight segment, and the colours indicate significant wave height according to the colour bars directly below. The black and white stars are the locations of the R/V Sikuliaq. Panels a and c are for Flight 2, taken on 16 October 2015 between 21:16 and 22:09 UTC. The SAR imagery at the sample region was taken at 16 October 2015 17:35:52 UTC (approximately 4 hours before the flight), and the background imagery in panel a was taken at 16 October 2015 04:00:06 UTC. Panel c is a zoomed view of the region outlined in cyan in panel a, and the letters A through E are the locations of the spectra in panels a-e in Fig. 5. Panels b and d are for Flight 4, taken on 23 October 2015 between 20:54 and 22:58 UTC. The background SAR imagery was taken at 23 October 2015 03:55:57 UTC (17 hours before the flight). Panel d also includes buoy data marked with diamond shapes, coloured with their observed H_s . T letters A through E are the locations of the spectra in panels a-e in Fig. 6. It is important to note that the labeling of “open water” and “sea ice” are simplifications; the open water areas contain some pancake and frazil ice, particularly for Flight 4, and the sea ice regions contain leads.

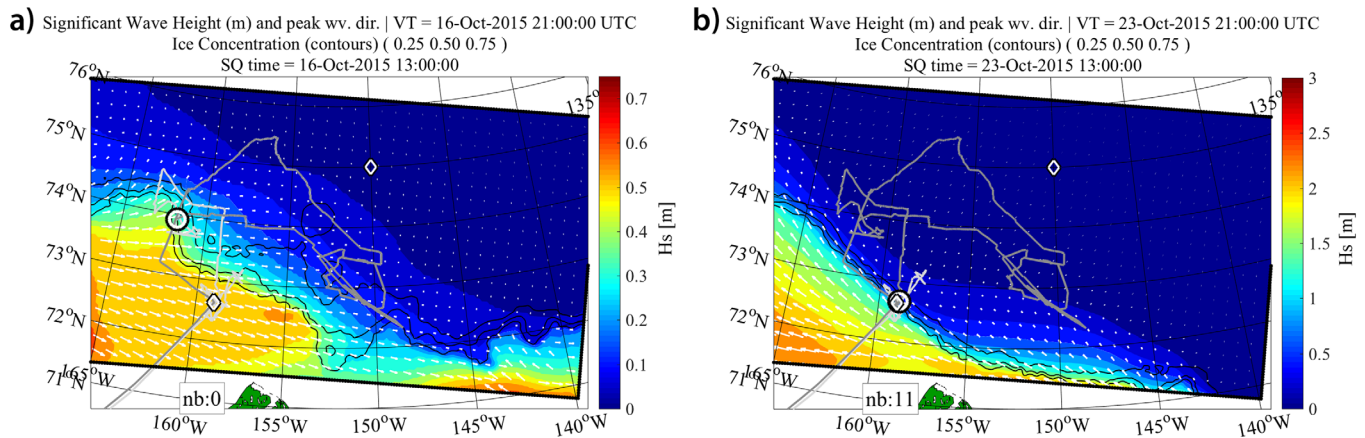


Figure 3. Modeled large-scale wave field. The colors correspond to the significant wave height, H_s , and the white arrows indicate the wave peak direction. The black lines indicate the 25%, 50%, and 75% ice contours, the gray lines indicate the track of the R/V Sikuliaq, and the black and white circles indicate the position of the R/V Sikuliaq during the sample period. Panel a is for Flight 2, Oct. 16, 2015, and panel b is for Flight 4, Oct. 23, 2015.

$$\phi(k) = \int_{-\pi}^{\pi} F(k, \theta) k d\theta. \quad (6)$$

It can be compared with the frequency spectrum, $\psi(\omega)$ by a transformation using the dispersion relation between k and ω . The wavenumber-dependent mean direction of the spectral peak, $\theta_p(k)$, can be calculated from $F(k)$ following

$$\theta_p(k) = \frac{\int_{-\pi}^{\pi} F(k, \theta)^q \theta d\theta}{\int_{-\pi}^{\pi} F(k, \theta)^q d\theta}, \quad (7)$$

where $q = 3$ is a constant, and the spectral spreading can be calculated using

$$\sigma(k) = \frac{\int_{-\pi/2}^{\pi/2} F(k, \theta) |\theta - \theta_p(k)| d\theta}{\int_{-\pi/2}^{\pi/2} F(k, \theta) d\theta}. \quad (8)$$

Directional wavenumber spectra are most commonly measured using remote sensing techniques, either airborne (e.g., Walsh et al., 1985), or satellite-based (e.g., Lyzenga et al., 1985). Wave retrieval from scanning lidar data is a powerful technique that has been used to measure the directional wave field in the open ocean (Hwang et al., 2000a, 2000b; Lenain & Melville, 2017; Romero & Melville, 2010), coastal regions (Reineman et al., 2009), and recently in the MIZ (Sutherland & Gascard, 2016).

The wave spectra extraction method used in this work was based on that presented in Sutherland and Gascard (2016) with two modifications: 1) The floe selection/elimination algorithm developed by Sutherland and Gascard (2016) was not used. The ice conditions during the SeaState cruise were predominantly first year ice, pancakes ice, or grease ice. This meant that the majority of the ice relief was of a similar scale to the measurement noise, and consequently negligible. Thus, the observed surface was assumed to be the sea surface. 2) Reciprocal flight paths covering the same wave field allowed removal of the 180 degree directional ambiguity otherwise present in the observations.

3.1. Data Preparation

The GPS and INS data were processed and integrated using the Applanix POS-PACKTM software package (<https://www.applanix.com/products/pospac-mms.htm>). This software incorporates a Kalman smoother to reduce overall positioning errors and smooth the step functions that would otherwise occur at changes of satellite constellation. The resulting aircraft trajectory and attitude data are then integrated with the lidar mirror angles and time-of-flight information through the Riegl Ri-PROCESSTM software package (<http://>

www.rieggl.com/products/software-packages/riprocess). This produces a lidar point-cloud in a local project planar coordinate system and then converted to the desired reference system, in this case EMG-08 vertical and WGS-84 UTM projection horizontal reference (northings and eastings). Cloud and sea-fog returns are edited from the files. Normally the point-clouds would be leveled by reference to any open water to remove GPS and geoid reference vertical errors but this was not necessary since the spectral calculations removed 2-D bias and trends from the data.

3.2. Spectral Calculation

Each 2 km flight segment was analyzed separately. The processing sequence was as follows: 1) Raw data from each flight segment was rotated from UTM coordinates into along-flight coordinates, where the x -coordinate is aligned with the mean direction of travel for the aircraft during that flight. 2) The ground swath for each flight segment was divided into 153.6×153.6 m square windows, centred on the mean flight axis, and 50% overlapping in the x -direction. 3) Elevation data within each window were gridded to a 256×256 point square grid. The value assigned to each grid point was the median of all elevation measurements within the 0.6×0.6 m window centred on the grid-point. Grid points where no data were present were filled by linear interpolation from the surrounding grid points. 4) Gridded elevation data were multiplied by a normalized 2-D Hann window function. 5) 2-D power spectra of each window were calculated individually using a 2D Fourier transform. 6) The spectra for all windows within each 2km flight segment were averaged to produce the mean power spectrum for each flight segment. 7) 2D power spectra were then rotated back to UTM coordinates (ENU).

After the 2D spectra were calculated, a correction for Doppler shift by the aircraft's movement was performed.

3.3. Doppler Shift Correction

When an aircraft flies over a surface wave field, it does so with a finite velocity. As such, the lidar does not record a "snapshot" of the sea surface. Instead each data point or scan line is slightly offset in time compared to the preceding one, and the observed surface wave field is Doppler shifted. The encountered (observed) wave frequencies, ω_e , are related to the true frequency, ω , by

$$\omega_e = \omega - \mathbf{U}_a \cdot \mathbf{k}, \quad (9)$$

where \mathbf{U}_a is the aircraft velocity. Walsh et al. (1985) showed that equation (9) could be re-written to show that the change in the wavenumber component in the along-flight direction is proportional to the ratio of the angular frequency and the aircraft speed. Written in vector form, Walsh et al. (1985)'s relation between true wavenumber, \mathbf{k} , and the encounter wavenumber, \mathbf{k}_e , is

$$\mathbf{k} = \mathbf{k}_e + \frac{\omega}{U_a} \widehat{\mathbf{U}}_a. \quad (10)$$

Here $\widehat{\mathbf{U}}_a$ is the unit vector in the direction of the aircraft velocity and $U_a = |\mathbf{U}_a|$ is the aircraft speed. In order to obtain the correct directional wavenumber spectra, Equation 10 must be solved for \mathbf{k} . In this work ω is related to k by the linear ice-free dispersion relation given in equation (A3) (the validity of this dispersion relation is discussed in Appendix A). Equation 10 can be then re-written as

$$\mathbf{k} = \mathbf{k}_e + \frac{1}{U_a} [gk \tanh(kH)]^{1/2} \widehat{\mathbf{U}}_a, \quad (11)$$

which was solved numerically for each wavenumber in the measured wavenumber spectra. The spectra were then re-gridded to a uniform wavenumber grid using linear interpolation.

3.4. Directional Ambiguity Resolution

Spatial snapshots of the sea surface elevation contain a 180° directional ambiguity, meaning that it is impossible to tell in which direction the waves are propagating. Typically the wave field has some directionality, and so the power spectrum calculated contains pairs of spectral peaks, 180° from one another. In each pair of peaks, there is one "true" peak in the direction of wave travel, and another "false" peak in the exact opposite direction. Doppler shifting due to the moving aircraft can be used to remove this ambiguity if the same (statistically) wave field is sampled with at least two flight directions (Walsh et al., 1985). This is because the Doppler correction moves the false peaks in the opposite direction from that in which they

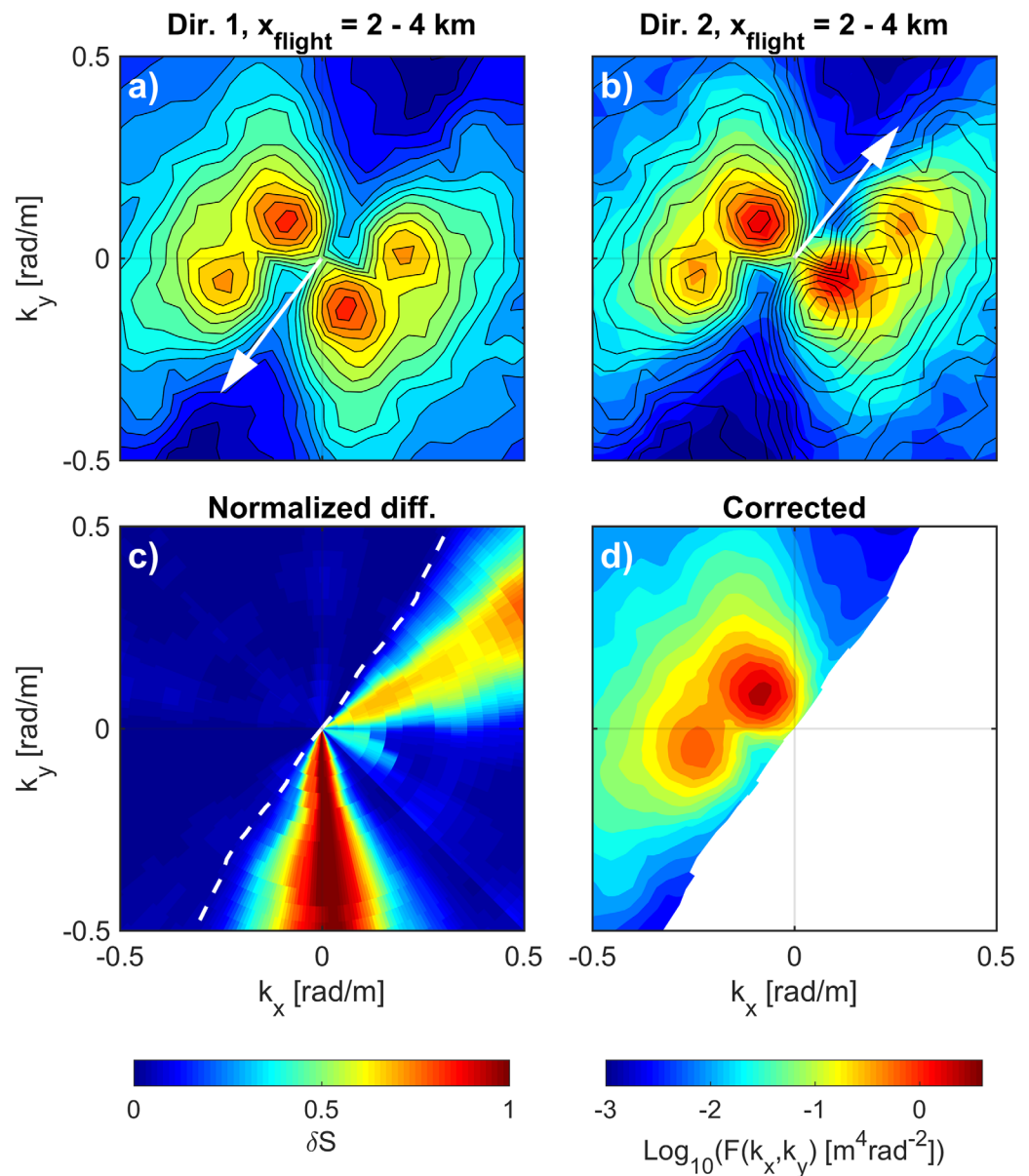


Figure 4. Directional ambiguity detection for a 2 km segment of Flight 4. The flight segment was centred at 72.533° N, 159.162° W, and the two passes were flown on 2017/10/23 at 22:00 UTC and 22:06 UTC, respectively. Panels a and b are the energy spectra with the Doppler-shift correction applied. The colours correspond to spectral energy, and the colour scale is that given in the lower right. The white arrows indicate the flight direction. The black contours are the contours of the spectrum in panel a, and are plotted in both panels a and b to highlight the difference between the two spectra. Panel c is the filtered, normalized difference between the spectra in panels a and b. The color scale is given in the lower left and varies between 0 and 1. Note that the upper left semicircle, the difference is uniformly low, whereas on the lower right semicircle, large differences are present. The white dashed line demarcates the boundary between the two regions. Panel d is the corrected spectrum; the sum of the spectra in panels a and b, with the energy in the false semicircle removed.

would have moved if they were real. An example of the processing is given in Figure 4. Panels a and b are the Doppler corrected spectra for two consecutive flights in opposite directions over an overlapping 2 km flight segment. It can be seen that, while the peaks on the upper-left hemisphere are in the same position in both cases, the lower right peaks are shifted considerably between images. This means that the upper-left peaks were the true peaks and the lower-right were the false. Panel c shows the normalized difference between the two spectra. The true hemisphere of the spectra was the side where the difference was uniformly low, and was determined for each wavenumber. The false hemispheres were then set to zero for

both spectra, and the true hemispheres were multiplied by a factor of two in order to conserve energy. The corrected spectrum (panel d) is then taken as the average of the two clipped spectra. During the SeaState campaign, this ambiguity resolution technique was applied to all cases where flights with reciprocal flight paths were present. The directions of the measured true spectral peaks were then used to infer the true peaks for nearby cases with only one flight direction.

In cases with waves with very broad spectral spreading, greater than 90° from the mean direction, this method for ambiguity resolution erroneously redistributes some of the spectral energy toward the spectral peak. In the extreme case where two true opposing spectral peaks are present, for example waves reflecting off a wall orthogonal to the propagation direction, this technique would redistribute all the energy in the direction of the strongest peak. These limitations are particularly important for studies of wave-ice interactions because ice floes are known to sometimes cause reflections that could cause exactly that type of spectrum.

4. Results

4.1. Spectral Evolution

Figures 5 and 6 show representative 2D directional wavenumber spectra for various locations along the aircraft track for flights 2 and 4, respectively. The locations where each of the spectra in those two figures were taken are indicated in Figure 2. In Figure 5, the two spectra from deepest inside the ice are panels b and c, both of which show a decrease in energy at high wavenumbers compared to the samples from open water. Figure 6 shows a sequence of spectra from deep inside the ice, panel a, to well outside, panel e. In that case, the wave energy at all wavenumbers and directions increases toward panel e.

The aforementioned behaviour is more clearly illustrated in Figures 7 and 8, where spectral parameters have been bin averaged in ice fetch, X_{ice} . Ice fetch is defined as the distance into the ice that waves have

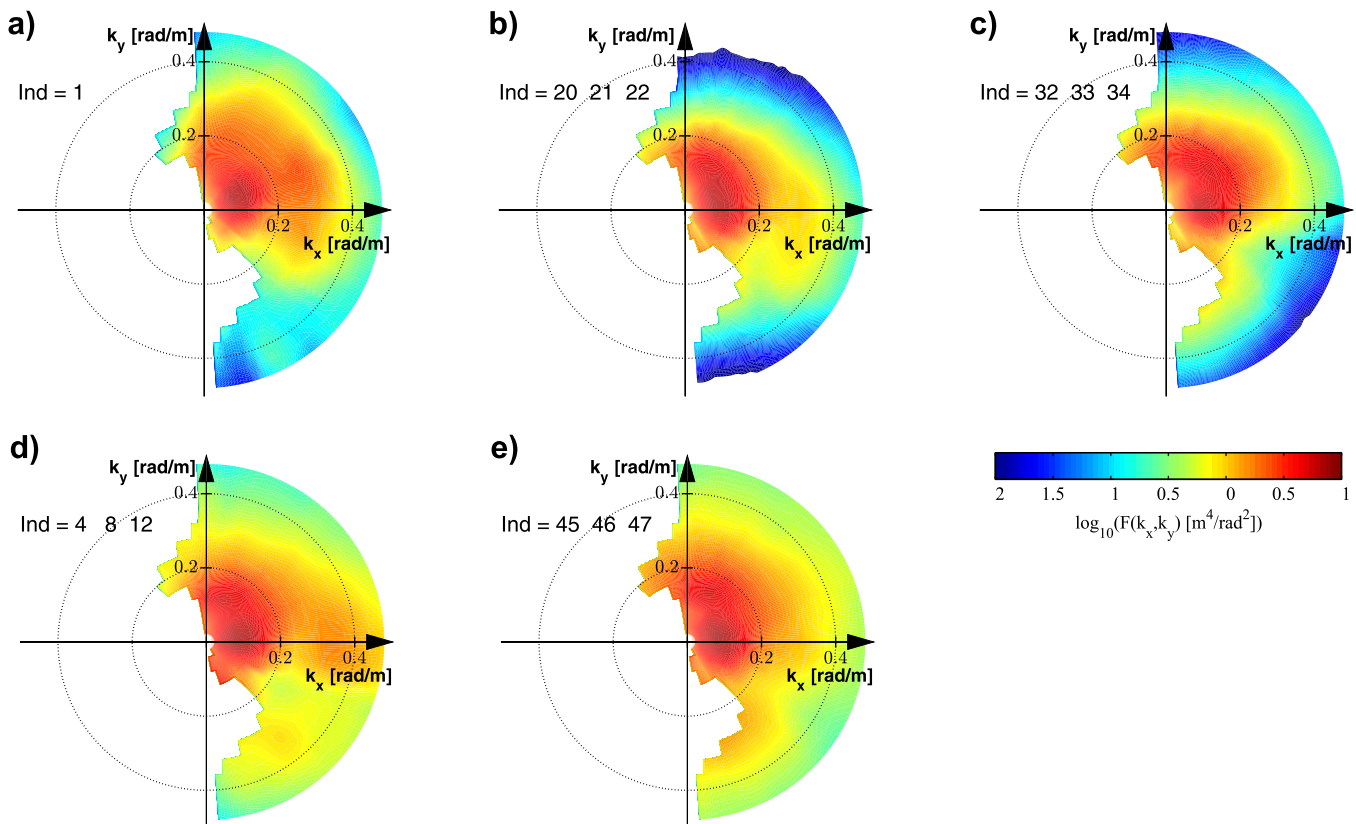


Figure 5. Spectra taken during Flight 2. Panel a corresponds to a 2km segment of flight nearest to the R/V Sikuliaq, and the rest of the panels are 6 km segments. The panel locations are indicated in Fig. 2.c. Panels b and c are from deepest inside the ice, and panels d and e are from off-ice near the ice edge. In this case, the wavefield was propagating in the on-ice direction approximately orthogonal to the mean ice edge.

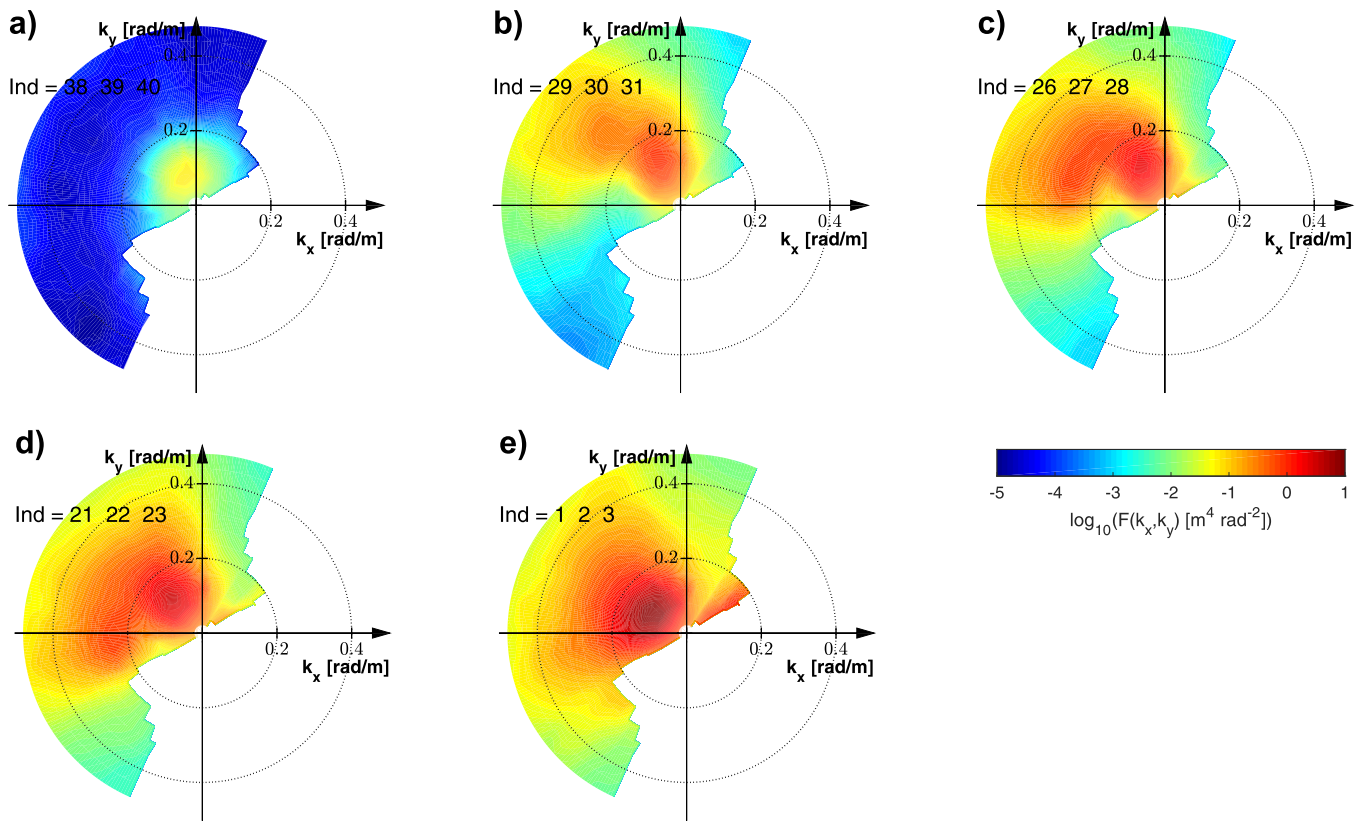


Figure 6. Spectra taken during Flight 4. Each spectrum corresponds to a 6km section of flight, and are labeled in Fig. 2.d. Panels a-e are along the transect starting deep inside the ice and extending into the lower concentration ice to the southwest. Two distinct wave components are present here (see text), and both wave components are clearly visible in panels b-d.

traveled in the direction of the spectral peak; the distance from the ice edge to the sample location along a line in the direction the peak of spectrum. At the ice edge, $X_{ice} \equiv 0$, for sample locations inside the ice, $X_{ice} > 0$, and for locations outside the ice, $X_{ice} < 0$. The ice edge was found using the SAR data shown in Figure 2; the images were expanded to maximum resolution and the ice boundaries were traced manually.

4.2. Comparison With Buoy Measurements

Comparison between the airborne data and more conventional in situ measurements can potentially provide insight into the strengths of both types of measurement. Flight 4 passed close to an array of Polar Scientific wave buoys, providing an opportunity to do just that. Figure 9 shows frequency spectra recorded by the lidar and the wave buoys. The measurements shown were separated by a maximum of 4 km in space and 1 hour in time.

The best geographic alignment between buoys and flights occurred for buoy 7 (Figure 9d) and the first pass over buoy 9 (Figure 9e, teal curve). In these cases, the buoys were within one swath width of the lidar pass, and collocated in time. The results within the range of validity are encouraging, with both measurements capturing very similar spectral peak structure and roll-off. The buoy data samples lower frequencies than the lidar because the lidar is limited to sampling wavelengths shorter than the swath width. However, in all cases the lidar system was capable of capturing the spectral peak.

The high frequency limit for the lidar system is set by the point resolution, and the frequency limit for the buoys is set by the response to the waves. The lidar was capable of capturing higher frequency waves (up to approximately 5 rad/s) than the buoys, when those waves had energy levels above the lidar noise level. This is illustrated in the spectral comparison for buoy 6 (Figure 9c), where the high frequency peak is well-resolved in the lidar data, but mostly missed by the buoy.

The buoy-lidar spectral comparisons highlight the spatial and temporal variability of the wave field. The spectral comparison for buoy 3 (Figure 9b) was collocated in space, but separated by an hour in time. In

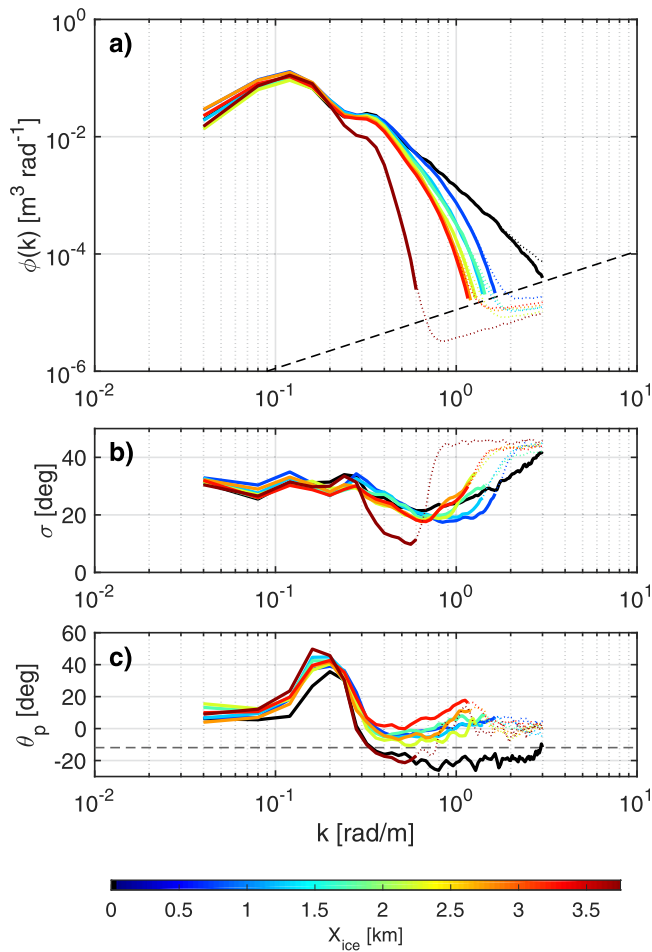


Figure 7. Integral spectral parameters for segment B-D (Fig. 7.c) of Flight 2. The data have been bin-averaged in ice fetch, X_{ice} . Each bin is 0.5 km, and the colours indicate the X_{ice} . The thick black lines indicate mean open water values. Panel a shows the omnidirectional wavenumber spectra (Eqn. 6). The thin dotted lines are the measured spectra, and the black dashed line is the approximate noise floor of the measurements. The solid lines are the spectra with the noise floor subtracted. Panel b is the spectral spreading, calculated using Eqn. 8, and panel c is the spectral peak direction, calculated using Eqn. 7, in ENU coordinates. In panels b and c, the dotted lines are the measurements and the solid lines highlight the region where the spectral energy levels are above the noise floor. The dashed grey line in panel c is the mean wind direction during the flight, measured at the R/V Sikuliaq.

that hour the spectral tail grew significantly. The second pass near buoy 9 (Figure 9d, orange curve) was collocated in time with the buoy measurements, but was near the maximum 4 km distance in space from the buoy. In that case also, the shape to the spectral tail changed significantly over a relatively short spatial scale. These small-scale differences are discussed further in Section 4.6.

Since the number of overlapping buoy and lidar measurements was relatively small, the buoy measurements were also compared against the model results discussed in Section 4.5. The differences between the buoy measurements and the model were consistent with the differences between the lidar measurements and the model, giving confidence in both measurement systems. Details of this comparison are given in the Supporting Information.

4.3. Wave Attenuation in Uniform Ice Conditions - Flight 2, B-D

Of the two cases analyzed, Flight 2 most closely resembled the configuration of the majority of previous wave-ice experiments, with waves propagating toward the ice in a direction nearly orthogonal to the ice edge.

Flight 2 was conducted in low forcing conditions, with the wind and wave fields approximately aligned. Although the omnidirectional spectrum for the incoming waves (black curve in Figure 7a) has the outward appearance of a wind-wave spectrum (e.g., Elfouhaily et al., 1997), the energy level of the observed spectrum is significantly lower. This is likely due to decreasing forcing.

Most previous work has shown that in uniform ice conditions waves attenuate exponentially in the MIZ, and that shorter waves are attenuated more rapidly than longer ones (e.g., Meylan et al., 2014; Wadhams et al., 1988). Figure 7a shows omnidirectional spectra for Flight 2 between points B and D (cf. Figure 2c), chosen due to the relatively uniform ice conditions. The data have been bin averaged so that each colored curve corresponds to a particular range of ice fetch, X_{ice} , with the blue curves from nearer the ice edge, and the red curves from deeper in the ice. Range bins are 500 m wide from the ice edge to 4 km. The data were analyzed in 2 km segments and the aircraft approached the ice edge obliquely, meaning that the change in X_{ice} was approximately 175 m during each segment. The expected spectral attenuation is clearly illustrated; as the wave field propagated into the ice, shorter waves at the tail of the spectra were attenuated most quickly (Figure 7).

The spectral dependence of attenuation is shown in Figure 10a. The wavenumber-dependent attenuation coefficient, $\alpha(k)$, is defined such that

$$\phi(\mathbf{x}_2; k) = \phi(\mathbf{x}_1; k) e^{-\alpha(k)[X_{ice}(\mathbf{x}_2) - X_{ice}(\mathbf{x}_1)]}. \quad (12)$$

Here, $\phi(\mathbf{x}; k)$ is the omni-directional wavenumber spectrum at location \mathbf{x} , $X_{ice}(\mathbf{x})$ is the ice fetch at that same location. The incoming wave field is assumed to be statistically homogeneous in space and time. For each discrete wavenumber, k_i , Eqn. 12 was solved for $\alpha(k_i)$. The colored lines in Figure 10a are attenuation coefficients calculated between consecutive ice fetch bins, and the black line was calculated by fitting all available data using a RANSAC least-squares estimate. Both the consecutive and overall estimates of $\alpha(k)$ show a strong dependence on k in the spectral tail. At lower wavenumbers, estimates of $\alpha(k)$ are noisy because the changes in spectral level between bins are smaller than the measurement confidence interval. The form of that dependence can be used to provide some insight into the physical mechanism responsible for the attenuation.

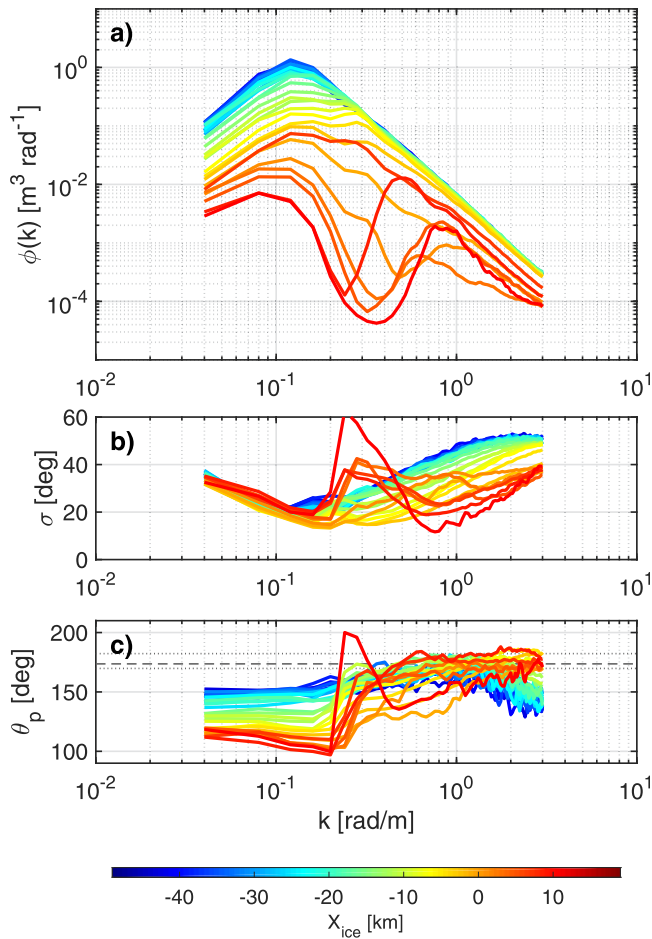


Figure 8. Integral spectral parameters for Flight 4, bin averaged in ice fetch, X_{ice} . The colours indicate ice fetch, with red being deepest inside the ice (largest X_{ice}), and blue being farthest away from the ice (smallest X_{ice}). Panel a gives the omnidirectional spectra (Eqn. 6), panel b gives the directional spreading (Eqn. 8), and panel c gives the mean wave direction (Eqn. 7).

X_{ice} bin by solving Eqn. 13 for ν_e . The results are shown in Figure 10b, plotted as functions of X_{ice} . For the first 3 km from the ice edge, eddy viscosities varied by approximately one order of magnitude around the mean of $\nu_e = 5.6 \times 10^{-6} \text{ m}^2 \text{ s}^{-1}$ (corresponding to the black line in Figure 10a). Between 3 and 3.5 km, ν_e abruptly increased to $2.4 \times 10^{-3} \text{ m}^2 \text{ s}^{-1}$. This jump was likely due to a change in ice type and/or thickness. Unfortunately the measurements necessary to quantify that change were not available.

The mean eddy viscosity of $\nu_e = 5.6 \times 10^{-6} \text{ m}^2 \text{ s}^{-1}$ is much lower than the majority of estimates in the literature, and the lowest inter-bin measurements approached the kinematic viscosity of seawater ($\nu = 2 \times 10^{-6} \text{ m}^2 \text{ s}^{-1}$ at 0°C). That ν_e should be well below the $\nu_e = 6.4 \times 10^{-4} \text{ m}^2 \text{ s}^{-1}$ observed by Sutherland and Gascard (2016) and the $\nu_e = 4 \times 10^{-4} \text{ m}^2 \text{ s}^{-1}$ estimated by Weber (1987) is unsurprising. Eddy viscosity depends strongly on ice roughness, and the data used for both of those experiments were taken in thick ice in large floes, which were expected to have very high under-ice roughness. In contrast, the current experiment took place in thin pancake ice which is expected to be much smoother. A more valuable comparison would then be with the work of Doble et al. (2015), who studied the dependence of α and ν_e on pancake ice thickness. They found that eddy viscosity was well correlated with ice thickness, h , and derived the following empirical relation,

$$\nu_e = e^{-5.26 + 5.64h} \quad (14)$$

Using typical pancake thickness values recorded by the R/V Sikuliaq on October 16 of approximately 10 cm, Eqn. 14 gives an eddy viscosity of $\nu_e = 9 \times 10^{-3} \text{ m}^2 \text{ s}^{-1}$, nearly 3 orders of magnitude larger the mean value

Scattering off floes is a well-known mechanism for wave attenuation in the MIZ (e.g., Squire, 2007; Squire et al., 1995). The strongest effects of scattering are observed for floe sizes as large, or larger than, the incident wave length (e.g., Dumont et al., 2011; Meylan & Squire, 1993). However, the size of the (largely pancake) ice floes under Flight 2 was generally near the resolution of the lidar, suggesting that any waves resolved by the lidar would not be expected to be scattered. Observations of spectral spreading appear to confirm this. Figure 7b shows spectral spreading defined as in Eqn. 8. Scattering models indicate that wave spectra should spread with distance into the ice, eventually reaching isotropy at some distance from the ice edge. In contrast, the observations show that the spectra narrowed slightly with distance into the ice. For these reasons, the focus of the following analysis is on a dissipative mechanism.

Several authors (e.g., Liu & Mollo-Christensen, 1988; Liu et al., 1991; Weber, 1987) have developed attenuation models that treat sea ice as a thin layer of highly viscous fluid floating on a less-viscous ocean. Assuming that $hk \ll 1$, where h is the ice thickness, and that the waves follow the linear deep water dispersion relation, Weber (1987) showed that the attenuation coefficient from such a viscous layer configuration can be written

$$\alpha(k) = \left(\frac{\nu_e^{1/2}}{\sqrt{2}g^{1/4}} \right) k^{7/4} \quad (13)$$

Here, ν_e is the “eddy viscosity” of ocean under the ice, which is not clearly defined. Weber (1987) used a value of $4 \times 10^{-4} \text{ m}^2 \text{ s}^{-1}$, and Sutherland and Gascard (2016) found a value of $\nu_e = 6.4 \times 10^{-4} \text{ m}^2 \text{ s}^{-1}$. Values for ν_e are expected to vary over at least 3 orders of magnitude, and are strongly dependent on ice thickness (e.g., Doble et al., 2015) and ice-bottom roughness.

Figure 10a has included $k^{7/4}$ curves to illustrate the power law dependence expected for viscous dissipation. The slope of the mean attenuation is within uncertainty of $k^{7/4}$, though it is also statistically indistinguishable from k^2 . Eddy viscosities were computed for each

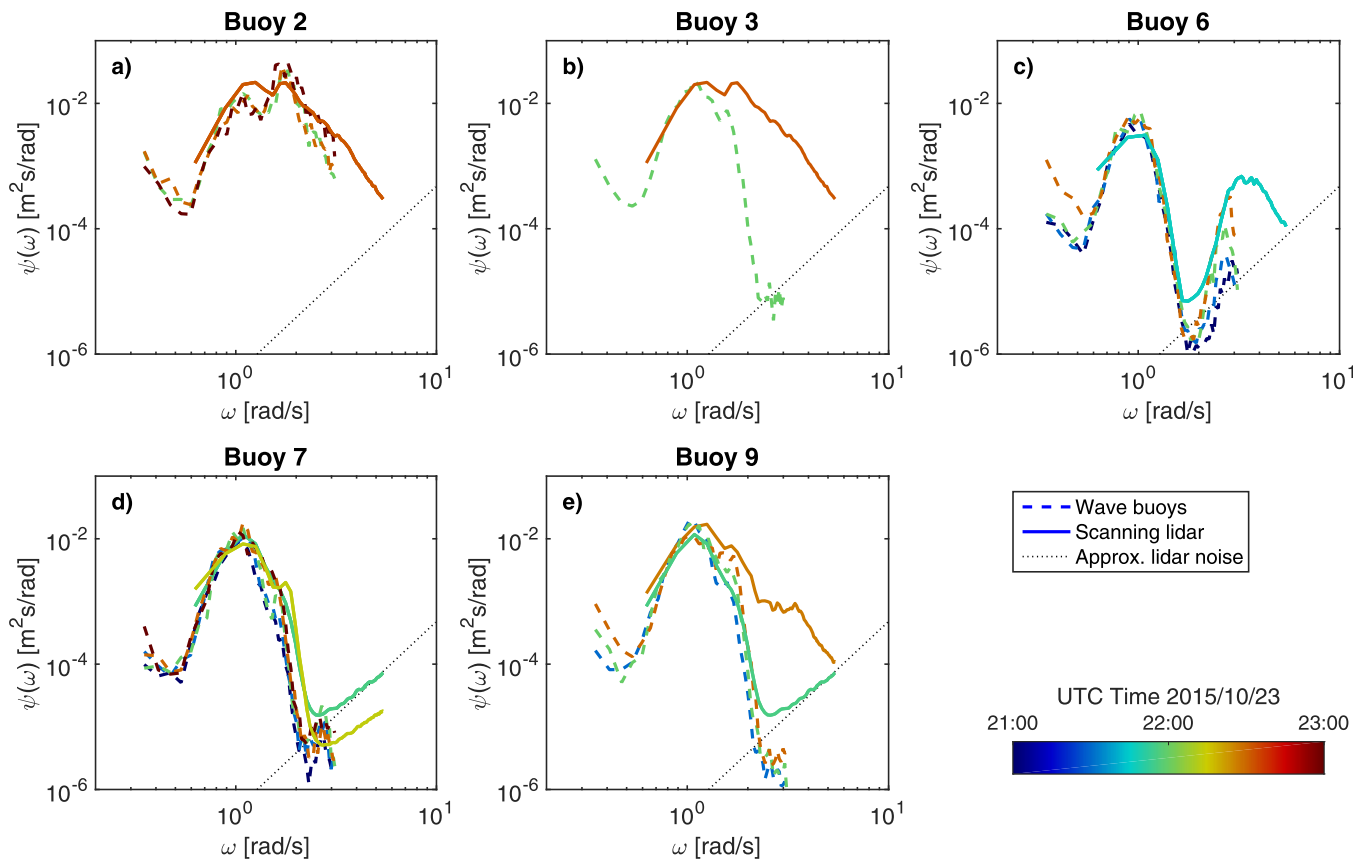


Figure 9. Comparison of frequency spectra from in situ buoy measurements and airborne scanning lidar. Panels a-e correspond to buoys 2, 3, 6, 7, and 9, respectively. The solid lines are lidar data taken within 4km of the buoy and each line corresponds to a 2km average segment. Omnidirectional wavenumber spectra (Eqn. 6) were transformed to frequency space using the linear open-water dispersion relation (equation A3). The dashed lines are the measured frequency spectra from the wave buoys, from within 1 hour of the aircraft pass. The line colour indicates the time of the sample following the color bar in the lower right; the more similar in colour a lidar sample and a buoy sample, the closer they are in time.

recorded here, and double the maximum inter-bin value. Comparison with other results from the literature provide similar disparities. For example, Newyear and Martin (1999) estimated water-side eddy viscosities in laboratory-generated grease ice to be more than three orders of magnitude larger than our mean values.

Clearly the mean eddy viscosities observed here are significantly lower those from the literature. Possible explanations for this disparity include: 1) Particularly low-turbulence conditions at the base of the ice layer. The pancake ice in this study was recently formed and, during this sampling period, weakly forced. This suggests that the ice bottom was likely extremely smooth, likely resulting in low eddy viscosities. 2) Wind input; in this case, winds were approximately aligned with the peak wave direction (c.f. Figure 7c), with a mean speed of 4.4 m/s, providing some forcing to the tail of the spectrum. The forcing of waves in sea ice by wind is not well understood, and there is currently no way to quantitatively estimate its effect on these measurements. However, if wind did add energy to the spectral tail inside the ice, it would reduce the apparent attenuation rates and eddy viscosities. 3) Horizontal variability of the incoming wave field: The aircraft in this case obliquely approached the ice edge, meaning that measurements at $X_{ice} = 0$ km were from approximately 15 km farther north than those at $X_{ice} = 3.5$ km. If the incoming wave field were more energetic, in the tail of the spectra where attenuation was observed, at the southern end of the transect than at the northern end, then our methodology would under-estimate attenuation and consequently eddy viscosity. Although concurrent off-ice measurements were not available, the numerical modeling results shown in Figure 3a can provide some insight into the large-scale behaviour of the incoming wave field. The flight discussed here was centred at approximately 73.5°N , 161°W , and a gradual decrease in wave energy with northward travel is indeed present, meaning that the incoming wave field would have had very slightly ($>5\%$) more energy for the measurements at $X_{ice} = 3.5$ km compared to those at $X_{ice} = 0$ km. However,

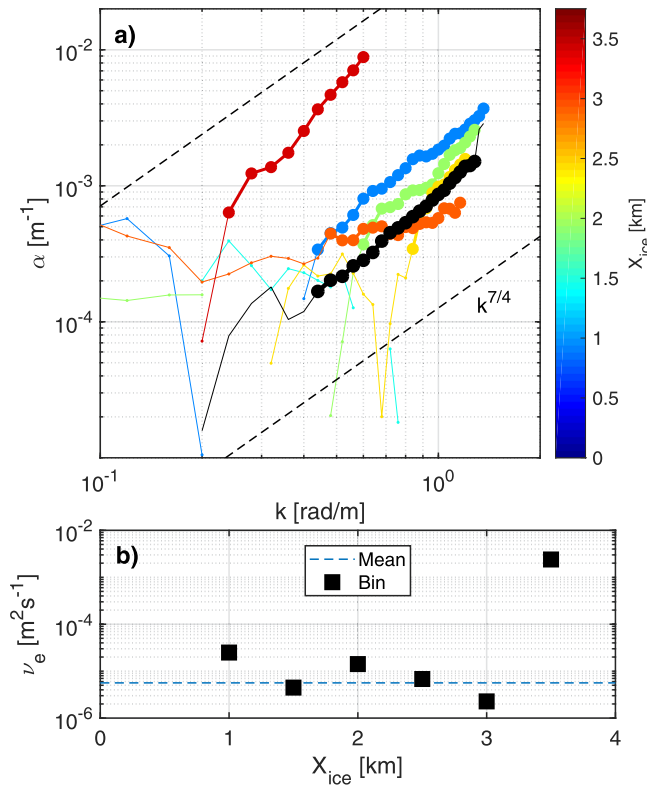


Figure 10. Wave attenuation during Flight 2. Panel a is the spectral attenuation, bin averaged as a function of ice fetch. Each colored line represents attenuation calculated between two consecutive bins, and the color indicates ice fetch. The section of each line that is highlighted by colored circles indicates the wavenumber range over which the attenuation is statistically significant. The solid black line is the mean spectral attenuation computed by fitting an exponential curve to all available data at each wavenumber. The region of that line highlighted by circles indicates the wavenumber range at which at least two ice fetch bins were available. The black dashed lines indicate curves with $k^{7/4}$ (c.f. equation 13). Panel b is the eddy viscosity plotted as a function of ice fetch. The black squares are values calculated for each ice fetch bin, and the dashed blue line is the mean value calculated from all available data (corresponding to the solid black line in panel a).

differences in modeled incoming wave energy over the spectral range at which attenuation was observed (high wavenumber tail) were not statistically significant. It is also worth noting that the resolution of the model was approximately 5 km (see Section 4.5), meaning that horizontal variability over the 15 km flight path in question was not well resolved. Smaller-scale variability, which would not be captured by the numerical simulations, could also have been present. For example, wave groups for waves at the peak of the observed spectra could have length scales of more than 500 m. If those waves modulated the shorter waves in the spectral tail, then it would be possible for them to affect the measured attenuation. Similarly unmeasured ice bands in open water could potentially produce a shadowing effect on the incoming wave field in some areas of the transect.

It is worth pointing out that although it is a popular modeling tool, eddy viscosity is often unsuitable for describing the dissipation of wave energy. The fundamental assumption inherent in an eddy viscosity formulation is that the local gradient of the mean flow determines the flux of momentum. In the case of simple shear flows, this works reasonably well. However this assumption only holds in the presence of wave motions if the spatial and temporal scales of the turbulence are much smaller than the scales of the wave motions. This criteria is not often met in the turbulence associated with the surface wave field.

4.4. Fetch Relation During Ice Formation - Flight 4

Flight 4 was conducted in off-ice forcing. Winds recorded at the R/V Sikuliaq were 11 m/s from 99° true, which means that they were obliquely off-ice, crossing the mean ice-edge at approximately 30°. The air temperature was -8.6°C . Since no other atmospheric observations are available during the flight, those values have been taken as representative of the entire flight path. The cold air temperatures resulted in a strongly unstable atmospheric boundary layer over open water and active ice formation, including the development of frazil and pancake ice. The off-ice forcing resulted in a divergence of the ice field near the ice edge causing leads to open, as well as the development of features like ice bands of newly-formed ice.

The significant wave height for each 2 km flight segment is indicated by color in Figure 2d, showing a clear trend toward higher waves with increasing distance from the ice edge. This is shown spectrally in Figure 6. Two distinct wave components are present here, though both are generated by the same easterly wind system: 1) Longer wavelength young swell propagating toward the NNW, roughly parallel to the ice edge. This is energy that is generated at angles strongly oblique to the easterly winds, but is facilitated by the large fetch available along this axis (along-ice). This low frequency wave component is present in all the images, but most visible in panel a (deepest in the ice), where it is the only system present. 2) Shorter off-ice wind waves growing in the wind direction, approximately WNW. This component becomes dominant in open water far from the ice edge. This spectral evolution can also be seen in the spectral integral parameters shown in Figure 8. The omnidirectional spectra (Figure 8a) contain two distinct peaks within the ice and near the ice edge (red). With increasing distance away from the ice edge into the open water, the wind wave peak moves to lower wavenumbers until it is indistinguishable from the swell peak. Figure 8c shows the directionality of the two systems, with the higher wavenumber wind-waves maintaining a constant direction, and the swell peak gradually shifting to the same direction.

Figure 11 shows the evolution of the wind wave energy with fetch. Fetch and energy have been nondimensionalized using wind speed, U_{10} , and gravitational acceleration, g , following Hasselmann et al. (1973) so that nondimensional fetch is

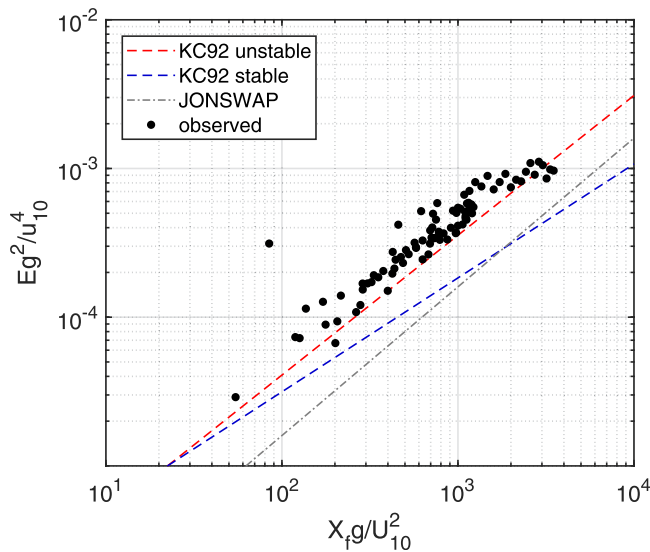


Figure 11. Development of wave energy as a function of fetch. The abscissa is nondimensional distance from the ice edge into open water and the ordinate is nondimensional wave energy. The black dots are data from this experiment. The dashed grey line is from the JONSWAP experiment (Hasselmann *et al.*, 1973), and the dashed red and blue lines are from Kahma and Calkoen (1992) for unstable and stable conditions, respectively.

$$X^* = -(g/U_{10}^2)X_f, \quad (15)$$

where X_f is the dimensional fetch (the distance that the waves traveled from the ice edge), and nondimensional energy is

$$E^* = (g/U_{10}^2)^2 E_{ww}. \quad (16)$$

In order to remove the contribution from swell from the fetch relation, E_{ww} was defined as

$$E_{ww} = E - E_0, \quad (17)$$

where E_0 is the mean wave energy within 500 m of the ice edge ($|X_{ice}| \leq 500$).

Various authors have observed that in standard fetch-limited scenarios, energy displays a power-law dependence on fetch, $E^* \sim X^{*d}$, where the empirically-determined d is in the approximate range of $0.7 < d < 1$ (Kahma & Calkoen, 1992). The lidar data show a similar functional dependence, with $d = 0.87$. Although the mean growth rate observed here is somewhat higher than the literature, it is within the scatter of previous measurements.

The presence of swell has been suggested as a potential mechanism for altering the growth rate, but little evidence for such an effect has been observed in the literature. Kahma and Calkoen (1992) found that fetch-limited wave energy growth rates showed significant dependence on boundary layer stability, with unstable conditions producing more rapid wave growth than stable conditions (indicated as red and blue dashed lines, respectively, in Figure 11). Since the conditions here were strongly unstable, it is expected that their spectral growth rate would be most similar to their unstable case, and potentially even more rapid.

If additional measurements confirm that the high growth rates observed here are indeed a feature of waves in ice-forming conditions, the cause of that elevation will be potentially important for our understanding of near-surface dynamics in high latitudes.

Higher growth rates are due to either increased wind input, decreased wave dissipation, or some combination thereof. Wind input in frazil generating conditions has not been well studied. However, a key characteristic of high near-surface frazil concentrations is a decrease in small-scale surface roughness, which causes the sea surface to appear oily, hence the colloquial term “grease ice.” Reduced surface roughness is associated with reduced wind input. If wind input is indeed decreased in the presence of frazil, then the observed high growth rate should be due to decreased dissipation of wave energy. The primary mechanism for wave energy dissipation in open water is turbulent kinetic energy (TKE) dissipation due to wave breaking (e.g., Sutherland & Melville, 2015). If wave breaking is reduced by the presence of frazil, then dissipation of wave energy would also be reduced. This would then result in increased wave growth rates.

The two most likely candidate mechanisms for the increased growth rate appear to be either strong atmospheric instability, or suppression of upper-ocean breaking by frazil. If the higher growth rates are due to atmospheric instability, and wave dynamics are otherwise unaffected, then the near-surface turbulence would be increased compared to less unstable conditions. However, if the higher growth rates are due to suppression of breaking, then near-surface turbulence would be decreased compared to frazil-free conditions. Although not trivial, including measurements of near-surface TKE dissipation in future field campaigns would help discern between these mechanisms. Unfortunately such measurements were not available for this work.

The two most likely candidate mechanisms for the increased growth rate appear to be either strong atmospheric instability, or suppression of upper-ocean breaking by frazil. If the higher growth rates are due to atmospheric instability, and wave dynamics are otherwise unaffected, then the near-surface turbulence would be increased compared to less unstable conditions. However, if the higher growth rates are due to suppression of breaking, then near-surface turbulence would be decreased compared to frazil-free conditions. Although not trivial, including measurements of near-surface TKE dissipation in future field campaigns would help discern between these mechanisms. Unfortunately such measurements were not available for this work.

4.5. Comparison With a Spectral Wave Model

As part of the Sea State project, spectral modeling of the wave field was performed (e.g., Rogers *et al.*, 2016) using the WAVEWATCH III[®] spectral model (The WAVEWATCH III[®] Development Group (WW3DG), 2016). Ice concentration fields were created from AMSR2 (Advanced Microwave Scanning Radiometer 2) swath data as described in Rogers *et al.* (2018) (henceforth denoted as R18). These fields are at relatively coarse

geographic resolution (10 km) and relatively fine temporal resolution (5.4 hours, on average). Directional spectra were calculated on an irregular grid with an approximately 5 km spatial resolution, with output at 30 minute temporal resolution. Maps of modeled wave fields corresponding to the two flight periods, including the input ice concentration, are given in Figure 3. For description of wind forcing, model settings, and further detail on the ice input and grids used, the reader is referred to R18. For the following analysis, the model spectra were bin-averaged in space and time to each of the 2 km flight segments. The spectra were then bin averaged in ice-fetch in the same manner as were the lidar spectra. Comparisons of the measured and modeled spectra are given in Figure 12. Several key features were observed.

Spectral peak wavenumbers were lower in the modeled data than in the observations; modeled peak wavenumbers were 18% lower than observations in Flight 2 and 50% lower in Flight 4. This could be due to the scale limitations imposed by the flight swath width and subsequent windowing; waves longer than the swath width were not captured. However, in all cases, the modeled wavelengths were short enough that the lidar would have been capable of measuring them. Furthermore, good agreement was found between the lidar and buoy spectral peaks (Sec. 4.2).

For Flight 2, the observations include a spectrum for which the ice fetch is zero, indicating an open water incoming wave spectrum. At this position, the model is showing strong suppression of the high frequency tail of the spectrum, suggesting that the open water position is misplaced as being inside the ice. At other locations, the observations reflect the strong wavenumber dependent spectral attenuation discussed in section 4.3. This is seen again in the model results, but the attenuation is overpredicted, probably because the model has the positions too far into the ice. It is worth noting that the observed attenuation occurred over a horizontal scale (approximately 4 km) that was smaller than the model resolution (5 km). As such, predictive skill is expected to be low. The overprediction of the damping of the high-frequency tail of the model spectra by sea ice caused the modeled H_s to be underestimated by approximately 18%.

For Flight 4, in the open water far from the ice edge, the spectral tail was well predicted, and bulk parameters were reasonably well estimated by the model, though there is an overprediction of low frequency energy. Farther than 20 km from the ice edge, average modeled and measured H_s differed by less than approximately 1%, and modeled peak wavenumbers were approximately 17% lower than the measurements. The good agreement in H_s is unfortunately probably just a result of fortuitous cancellation of errors, with an overprediction of the longer waves from the southeast, and underprediction of the shorter waves generated by off-ice winds from the east. At most, if not all, of the measurement locations, the model showed significantly more low-frequency energy than was observed, and at higher wavenumbers, the model did not show the wind wave

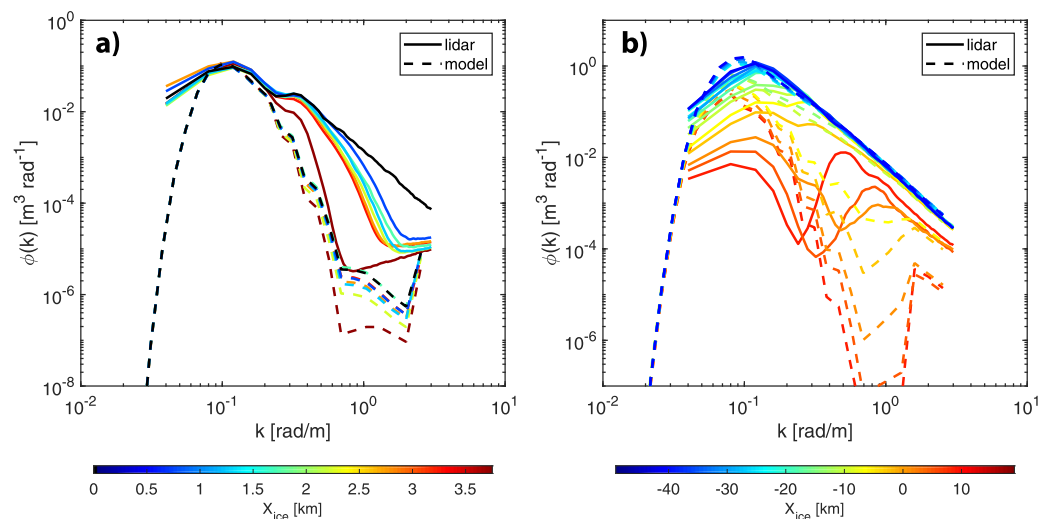


Figure 12. Comparisons of modeled (dashed lines) and measured (solid lines) wave spectral evolution. Panel a is from Flight 2; the colours indicate ice fetch and black is the average of all off-ice locations. Note that the observed spectra reach the noise floor of the system (c.f. Figure 7). Panel b is from Flight 4; the colours indicate ice fetch, where blue is farthest in the off-ice direction (southwest) and red is deepest inside the ice.

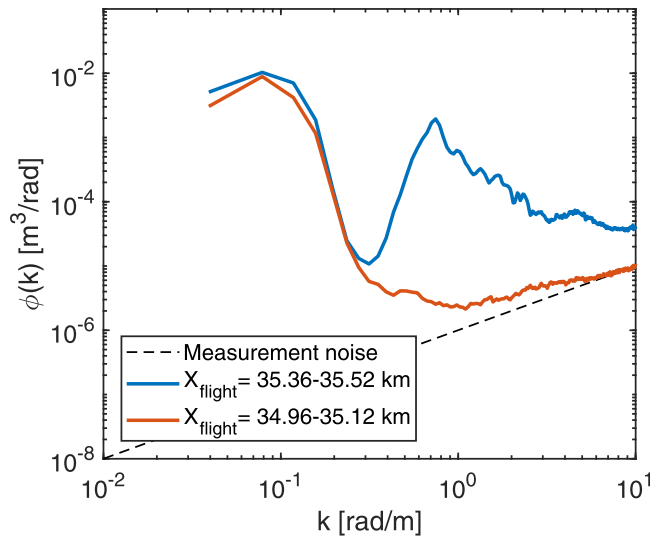


Figure 13. Comparison of omnidirectional spectra from two locations in Fig. 1.a. The centres of the spectral calculation windows are separated by 400 m in the direction of the flight path. The orange curve is from the left side of the image in Fig. 1.a (thicker ice), and the blue curve is from the right side of the image (frazil and open water). The black dashed line is the noise floor of the measurements.

peak visible in lidar spectra. The former suggests that the model is either overpredicting the generation of wave energy strongly oblique to the wind direction, or is underpredicting the ice along the ice edge to the southeast, that being the up-wave direction of this longer-wave component. The overprediction of low frequencies resulted in the model overestimating H_s by 120% inside the ice edge. The underprediction of the high frequencies in the model indicates that it is either overpredicting the suppression of windsea growth by sea ice, or overpredicting the dissipation of the windsea by sea ice. Either could be caused by an overprediction of ice locally. The possibility (or probability) that the model is afflicted by ice concentration that is too high locally and too low to the southeast highlights the extreme difficulty of wave prediction so near the ice edge, which in fact is one of the main findings of R18. The main findings discussed here were also present in a comparison of buoy data and model results, as described in the Supporting Information.

The differences between modeled and observed wave conditions found here would be expected to be significant for operational activities near the ice boundary. The first-order cause of the differences at high wavenumbers appears to be inaccurate estimates of the ice boundary location; the spectral tail is extremely sensitive to small-scale ice conditions over scales smaller than a few kilometres.

4.6. Small-Scale Features and Wave Evolution

The analysis up to this point has been conducted on spectra averaged over 2 km sections of the flight path, sampling designed to capture the large-scale variability of the wave field. However, ice features and the associated changes to the wave field can in some cases evolve over much smaller scales. Figure 1a, for example, shows a rapid transition from open water (right side of image) to sea ice (left). At the boundary, an agglomeration of floes a few tens of centimetres thick, with local ridging to greater than one metre, caused the short waves to be immediately attenuated. Figure 13 shows spectra from before and after the waves have passed across that ice boundary. While the swell peak (at

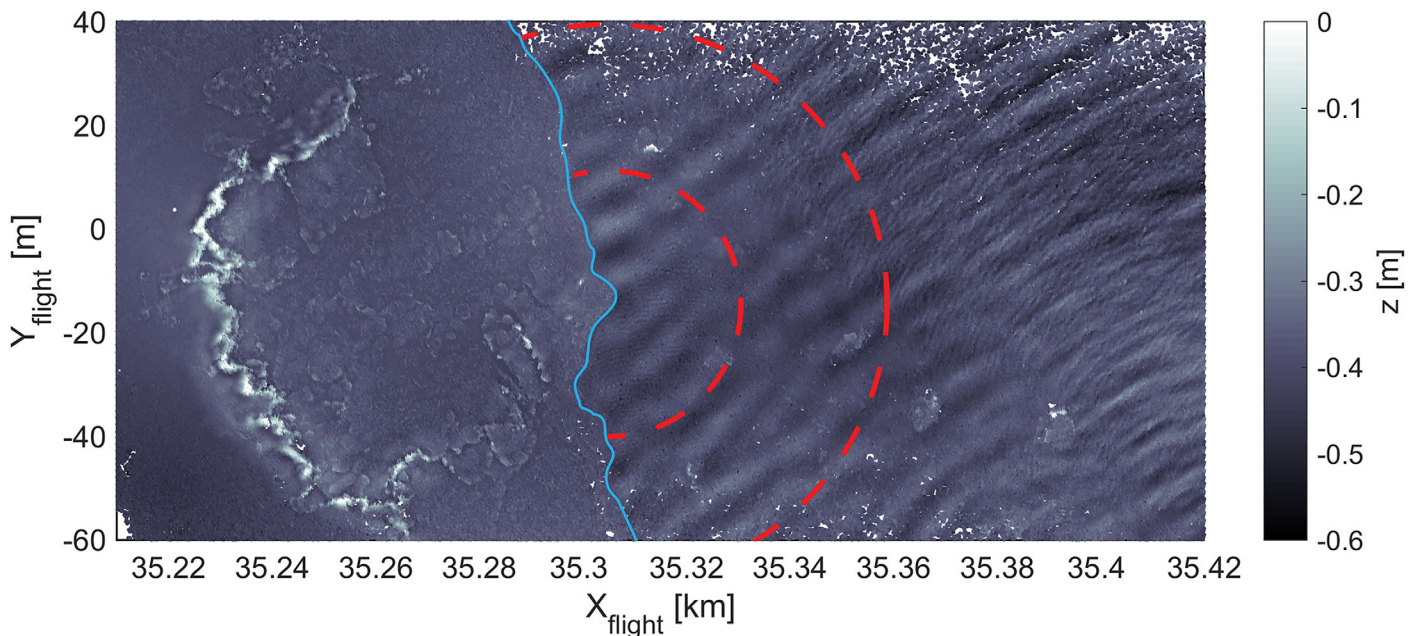


Figure 14. Raw lidar elevation data taken during Flight 4; zoom of the centre region of Figure 1.a. The colour indicates vertical elevation. The jagged white line on the left side of the image is an ice ridge. The ice-water boundary is at approximately $X_{flight} = 35.3$ km and has been traced with the light blue line. The red dashed circles highlight the ring waves.

approximately $k = 0.08$ rad/m, $\lambda = 80$ m) was unchanged to within the uncertainty of the spectral estimate, the wind sea peak (at approximately $k = 0.8$ rad/m, $\lambda = 8$ m) entirely disappeared inside the ice.

Furthermore, in contrast to the large-scale observations (Section 4.3), some of attenuation appears to be reflection-driven. The ring-shaped waves radiating from a point at approximately $X_{flight} = 35.3$ km, $Y_{flight} = -10$ m are a tell-tale indicator of reflections from an ice feature at that point. Closer inspection, Figure 14, reveals that those reflections are associated with ice floes with horizontal scales the same scale and larger than the scale of the short wind waves.

Short wind waves such as the ones shown here are unlikely to be important for ice breakup or have major implications for marine structures. In this case, the significant wave height associated with the wind waves was only 14 cm. However their implications for air-sea interactions are significant. Short wave breaking and the associated near-surface turbulence has been shown to be responsible for a large fraction of the transfer of energy, momentum, and mass between the atmosphere and the ocean (Sutherland & Melville, 2015). Even in mostly ice-covered waters, such exchanges in low-fetch polynya are thought to be extremely important for overall gas fluxes in the Arctic Ocean (Else et al., 2011). Thus clearly understanding wave field evolution in rapidly changing ice conditions will be important for future studies of air-sea exchanges in polar regions.

5. Conclusions

This work produced high-quality estimates of directional wavenumber spectra in the MIZ. Analysis was performed on 234 independent 2 km flight segments, extending from approximately 15 km inside the ice

edge to 55 km outside it. Two cases were studied: on-ice waves attenuated by sea ice, and developing waves in off-ice winds and ice forming conditions. In thin pancake ice, wave attenuation was observed to be largely dissipative, with average under-ice eddy viscosities approaching the molecular viscosity. The wave growth rate in ice forming conditions was observed to be slightly higher than those provided by fetch relations from the literature. The significance of this difference, and the reasons for it, have important implications for upper-ocean turbulence in polar regions, but are not yet resolved.

A reoccurring theme in this work is that small-scale ice features with high horizontal variability affect the development and attenuation of surface waves dramatically. Airborne scanning lidar is an excellent tool for capturing the wave field at the relevant scales, and would benefit, in the future from the inclusion of additional video and infrared sensors (e.g., Melville et al., 2016) for measuring, for example surface temperature and floe sizes.

Appendix A: Dispersion Relation in the MIZ

The motions of waves in space and in time are related by the dispersion relation. The linear dispersion relation for waves propagating in water with depth H , and covered by a thin elastic plate (sea ice) with thickness, h , can be written as (e.g., Liu & Mollo-Christensen, 1988)

$$\omega^2 = \left[gk + \underbrace{\frac{Yh^3k^5}{12(1-s^2)\rho_w}}_{\text{Flexure}} - \underbrace{\frac{Phk^3}{\rho_w}}_{\text{Compression}} \right] \left(\underbrace{\frac{\rho_l}{\rho_w}hk}_{\text{Mass loading}} + \coth(kH) \right)^{-1}. \quad (\text{A1})$$

Here g is gravitational acceleration, ρ_w is the water density, ρ_l is the ice density, Y is the Young's modulus of the floating ice, s is Poisson's ratio for the ice, and P is the compressive stress in the ice pack, which depends heavily on ice type.

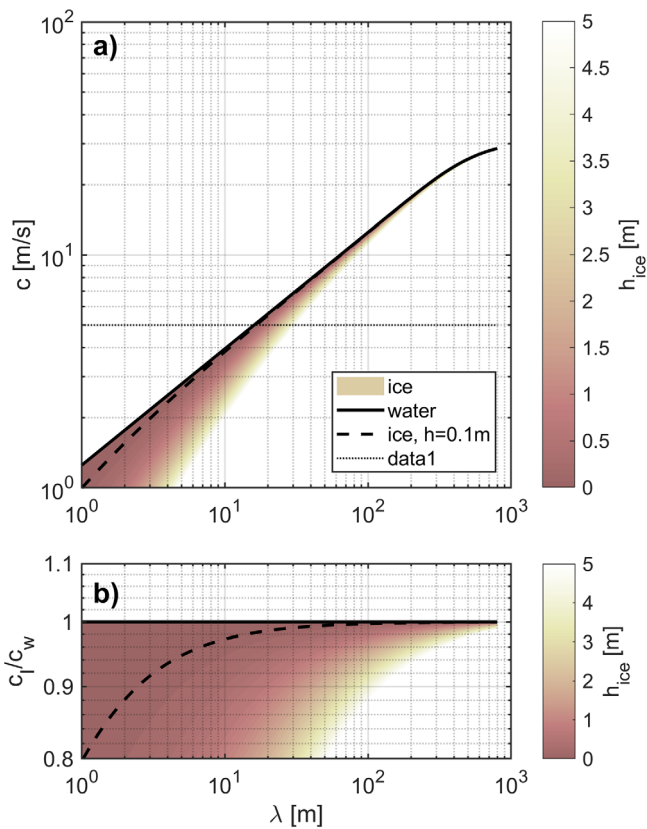


Figure A1. Dispersion relation calculated using equation (A2) for varying values of ice thickness, h . Panel a) gives the wave phase speed, c , as a function of wave length, λ . The solid black line is the open water dispersion relation ($h = 0$), and the dashed black line is for $h = 0.1$ m. The thin horizontal dashed line indicates 5 m/s, the approximate lower limit of significant Doppler shifting by the measurement platform. Panel b) is the ratio of the ice-covered phase speed to the open water phase speed, c_i/c_w . The black dashed line is for ice with $h = 0.1$ m.

The lidar measurements were taken near the ice edge, where the ice was largely small broken chunks, or pancake ice. The scale of the pancakes is implicitly limited to scales much less than the wavelengths in question (e.g., Doble et al., 2015), and the compression resistance of ice jumbles is significantly less than that in solid ice. Consequently, the flexure and compression terms in equation (A1) can be neglected, and equation (A1) simplifies to

$$\omega^2 = gk \left(\frac{\rho_l}{\rho_w} hk + \coth(kH) \right)^{-1}, \quad (\text{A2})$$

which only differs from the open water dispersion relation by the mass-loading term. Figure A1 shows wave phase speeds plotted as a function of wave length for various values of h .

During the Sea State campaign, measurements of pancake thickness were made several times daily. In all cases, the mean thickness was less than 0.1 m. Consequently, as can be seen in Figure A1, the wave phase speed in ice, c_i , differed from the phase speed in open water, c_w , by less than 10% for waves with length longer than approximately 3 m. The Doppler shift correction to spectra measured using airborne lidar is negligible for waves with phase speeds much less than the aircraft speed, $c_i \ll U_a$. In this experiment, the mean aircraft velocity was approximately 50 m/s. Consequently Doppler shift correction is required for waves with phase speeds greater than approximately 5 m/s, corresponding to wavelengths greater than approximately 15 m. This means that, during this experiment, for the purposes of Doppler correction, the dispersion relation never differed significantly its open-water form. The mass loading term in equation (A2) was consequently neglected, and all spectral corrections used the standard form for the linear open-water dispersion relation,

$$\omega^2 = gk \tanh(kH). \quad (\text{A3})$$

It is important to note that the assumption of a form for the dispersion relation is a key element of the processing presented here. In this analysis, due to measured in situ conditions, it was possible to neglect all dispersive effects of the floating ice layer and assume that the observed waves followed equation (A3). This assumption is not universally valid; clearly in cases with larger diameter or thicker floes or more compressed ice, additional terms in equation (A1) must be retained. Nonetheless, the range of conditions over which the open water dispersion relation has been observed to hold, is somewhat wider than expected. For example, Sutherland and Rabault (2016) observed waves with wavelengths between 7 and 50 m wavelengths propagating through approximately 0.5 m thick land-fast ice. They found that, except for a brief period when the waves first arrived, the open-water dispersion relation was followed.

Acknowledgments

These data were taken as part of the Office of Naval Research Sea State project. The aircraft costs were funded through the NRL Platform Support Program and the ONR Sea State DRI. PS was supported by the CNES project WAVE-ICE, and by the "Laboratoire d'Excellence" LabexMER (ANR-10-LABX-19), co-funded by a grant from the French government under the program "Investissements d'Avenir". JB was supported by the ONR/NRL base program in Sea Ice Physics (Program Element 61153N), and grant number N0001415WX01874 under the ONR Sea State and Boundary Layer Physics of the Emerging Arctic Ocean Departmental Research Initiative (DRI). The numerical modeling was supported by ONR grant No. N0001414WX20022 to WER. The buoy measurements and contributions by MD and PW were supported by ONR grant No. N00014-13-1-0290 to MD and PW. The Sea State data are available from the project page: www.apl.uw.edu/arcticseastate.

References

- Arduin, F., Collard, F., Chapron, B., Girard-Arduin, F., Guitton, G., Mouche, A., & Stopa, J. (2015). Estimates of ocean wave heights and attenuation in sea ice using the sar wave mode on sentinel-1a. *Geophysical Research Letters*, 42, 2317–2325. <https://doi.org/10.1002/2014GL062940>
- Arduin, F., Sutherland, P., Doble, M., & Wadhams, P. (2016). Ocean waves across the arctic: Attenuation due to dissipation dominates over scattering for periods longer than 19s. *Geophysical Research Letters*, 43, 5775–5788. <https://doi.org/10.1002/2016GL068204>
- Arduin, F. J., Stopa, B., Chapron, F., Collard, M., Smith, J., Thomson, M., et al. (2017). Measuring ocean waves in sea ice using SAR imagery: A quasi-deterministic approach evaluated with sentinel-1 and in situ data. *Remote Sensing of Environment*, 189, 211–222. <https://doi.org/10.1016/j.rse.2016.11.024>
- Asplin, M. G., Galley, R., Barber, D. G., & Prinsenber, S. (2012). Fracture of summer perennial sea ice by ocean swell as a result of arctic storms. *Journal of Geophysical Research*, 117, C06025. <https://doi.org/10.1029/2011JC007221>
- Benetazzo, A. (2006). Measurements of short water waves using stereo matched image sequences. *Coastal Engineering*, 53, 1013–1032.
- Campana, J., Terrill, E. J., & de Paolo, T. (2017). A new inversion method to obtain upper-ocean current-depth profiles using x-band observations of deep-water waves. *Journal of Atmospheric and Oceanic Technology*, 34(5), 957–970. <https://doi.org/10.1175/JTECH-D-16-0120.1>
- Campbell, A. J., Bechle, A. J., & Wu, C. H. (2014). Observations of surface waves interacting with ice using stereo imaging. *Journal of Geophysical Research: Oceans*, 119, 3266–3284. <https://doi.org/10.1002/2014JC009894>
- Collins, C. O., Rogers, W. E., Marchenko, A., & Babanin, A. V. (2015). In situ measurements of an energetic wave event in the arctic marginal ice zone. *Geophysical Research Letters*, 42, 1863–1870. <https://doi.org/10.1002/2015GL063063>
- Doble, M. J., & Bidlot, J.-R. (2013). Wave buoy measurements at the antarctic sea ice edge compared with an enhanced ECMWF WAM: Progress towards global waves-in-ice modelling. *Ocean Modelling*, 70, (0), 166–173. <https://doi.org/10.1016/j.ocemod.2013.05.012>
- Doble, M. J., Coon, M. D., & Wadhams, P. (2003). Pancake ice formation in the weddell sea. *Journal of Geophysical Research*, 108(C7), 3209. <https://doi.org/10.1029/2002JC001373>
- Doble, M. J., De Carolis, G., Meylan, M. H., Bidlot, J.-R., & Wadhams, P. (2015). Relating wave attenuation to pancake ice thickness, using field measurements and model results. *Geophysical Research Letters*, 42, 4473–4481. <https://doi.org/10.1002/2015GL063628>
- Doble, M. J., & Wadhams, P. (2006). Dynamical contrasts between pancake and pack ice, investigated with a drifting buoy array. *Journal of Geophysical Research*, 111, C11S24. <https://doi.org/10.1029/2005JC003320>

- Dumont, D., Kohout, A., & Bertino, L. (2011). A wave-based model for the marginal ice zone including a floe breaking parameterization. *Journal of Geophysical Research*, *116*, C04001. <https://doi.org/10.1029/2010JC006682>
- Elfouhaily, T., Chapron, B., Katsaros, K., & Vandemark, D. (1997). A unified directional spectrum for long and short wind-driven waves. *Journal of Geophysical Research*, *102*, 15,781–15,796.
- Else, B. G. T., Papakyriakou, T. N., Galley, R. J., Drennan, W. M., Miller, L. A., & Thomas, H. (2011). Wintertime CO_2 fluxes in an arctic polynya using eddy covariance: Evidence for enhanced air-sea gas transfer during ice formation. *Journal of Geophysical Research: Oceans*, *116*, C00G03. <https://doi.org/10.1029/2010JC006760>
- Hasselmann, K., Barnett, T., Bouws, E., Carlson, H., Cartwright, D., Enke, K., et al. (1973). Measurements of wind-wave growth and swell decay during the joint north sea wave project (JONSWAP). *Ergänzungsheft zur Deutschen Hydrographischen Zeitschrift*, *8*, 1–95.
- Hayes, D. R., Jenkins, A., & McPhail, S. (2007). Autonomous underwater vehicle measurements of surface wave decay and directional spectra in the marginal sea ice zone. *Journal of Physical Oceanography*, *37*, 71–83.
- Herbers, T. H. C., Jessen, P. F., Janssen, T. T., Colbert, D. B., & MacMahan, J. H. (2012). Observing ocean surface waves with gps-tracked buoys. *Journal of Atmospheric and Oceanic Technology*, *29*, 944–959. <https://doi.org/10.1175/JTECH-D-11-00128.1>
- Hwang, P. A., Wang, D. W., Walsh, E. J., Krabill, W. B., & Swift, R. N. (2000a). Airborne measurements of the wavenumber spectra of ocean surface waves. part i: Spectral slope and dimensionless spectral coefficient. *Journal of Physical Oceanography*, *30*(11), 2753–2767.
- Hwang, P. A., Wang, D. W., Walsh, E. J., Krabill, W. B., & Swift, R. N. (2000b). Airborne measurements of the wavenumber spectra of ocean surface waves. part ii: Directional distribution. *Journal of Physical Oceanography*, *30*(11), 2768–2787.
- Kahma, K. K., & Calkoen, C. J. (1992). Reconciling discrepancies in the observed growth of wind-generated waves. *Journal of Physical Oceanography*, *22*(12), 1389–1405.
- Kohout, A. L., & Meylan, M. H. (2008). An elastic plate model for wave attenuation and ice floe breaking in the marginal ice zone. *Journal of Geophysical Research*, *113*, C09016. <https://doi.org/10.1029/2007JC004434>
- Kohout, A. L., Williams, M. J. M., Dean, S. M., & Meylan, M. H. (2014). Storm-induced sea-ice breakup and the implications for ice extent. *Nature*, *509*, 604–607. <https://doi.org/10.1038/nature13262>
- Lenain, L., & Melville, W. K. (2017). Measurements of the directional spectrum across the equilibrium saturation ranges of wind-generated surface waves. *Journal of Physical Oceanography*, *47*(8), 2123–2138. <https://doi.org/10.1175/JPO-D-17-0017.1>
- Liu, A. K., Holt, B., & Vachon, P. W. (1991). Wave propagation in the marginal ice zone: Model predictions and comparisons with buoy and synthetic aperture radar data. *Journal of Geophysical Research: Oceans*, *96*, 4605–4621. <https://doi.org/10.1029/90JC02267>
- Liu, A. K., & Mollo-Christensen, E. (1988). Wave propagation in a solid ice pack. *Journal of Physical Oceanography*, *18*, 1702–1712.
- Longuet-Higgins, M. S., Cartwright, D. E., & Smith, N. D. (1963). Observations of the directional spectrum of sea waves using the motions of a floating buoy, Ocean Wave Spectra Proceedings of a Conference May 1961, Easton, Maryland, National Academy of Sciences.
- Lyzenga, D. R., Shuchman, R. A., Lyden, J. D., & Rufenach, C. L. (1985). Sar imaging of waves in water and ice: Evidence for velocity bunching. *Journal of Geophysical Research*, *90*, 1031–1036.
- Masson, D., & Leblond, P. H. (1989). Spectral evolution of wind-generated surface gravity waves in a dispersed ice field. *Journal of Fluid Mechanics*, *202*, 43–81. <https://doi.org/10.1017/S0022112089001096>
- Melville, W. K., Lenain, L., Cayan, D. R., Kahru, M., Kleissl, J. P., Linden, P. F., & Statom, N. M. (2016). The modular aerial sensing system. *Journal of Atmospheric and Oceanic Technology*, *33*(6), 1169–1184. <https://doi.org/10.1175/JTECH-D-15-0067.1>
- Meylan, M., & Squire, V. A. (1993). Finite-floe wave reflection and transmission coefficients from a semi-infinite model. *Journal of Geophysical Research*, *98*, 12537–12542. <https://doi.org/10.1029/93JC00940>
- Meylan, M. H., Bennetts, L. G., & Kohout, A. L. (2014). In situ measurements and analysis of ocean waves in the antarctic marginal ice zone. *Geophysical Research Letters*, *41*, 5046–5051. <https://doi.org/10.1002/2014GL060809>
- Newyear, K., & Martin, S. (1999). Comparison of laboratory data with a viscous two layer model of wave propagation in grease ice. *Journal of Geophysical Research*, *104*, 7837–7840. <https://doi.org/10.1029/1999JC900002>
- Phillips, O. M. (1977). *The Dynamics of the Upper Ocean*. Cambridge, UK: Cambridge University Press.
- Reineman, B. D., Lenain, L., Castel, D., & Melville, W. K. (2009). A portable airborne scanning lidar system for ocean and coastal applications. *Journal of Atmospheric and Oceanic Technology*, *26*(12), 2626–2641. <https://doi.org/10.1175/2009JTECH0703.1>
- Robin, G. D. Q. (1963). Wave propagation through fields of pack ice. *Philosophical Transactions of the Royal Society of London A: Mathematical, Physical and Engineering Sciences*, *255*(1057), 313–339. <https://doi.org/10.1098/rsta.1963.0006>
- Rogers, W. E., Posey, P., Li, L., & Allard, R. A. (2018). Forecasting and hindcasting waves in and near the marginal ice zone: Wave modeling and the ONR “Sea State” field experiment, *NRL Memorandum Report, NRL/MR/7320–18–9786*, 179 pp. Retrieved from <https://www7320.nrlssc.navy.mil/pubs.php>
- Rogers, W. E., Thomson, J., Shen, H. H., Doble, M. J., Wadhams, P., & Cheng, S. (2016). Dissipation of wind waves by pancake and frazil ice in the autumn beaufort sea. *Journal of Geophysical Research: Oceans*, *121*, 7991–8007. <https://doi.org/10.1002/2016JC012251>
- Romero, L., & Melville, W. K. (2010). Airborne observations of fetch-limited waves in the gulf of tehuatepec. *Journal of Physical Oceanography*, *40*, 441–465.
- Schulz-Stellenfleth, J., & Lehner, S. (2002). Spaceborne synthetic aperture radar observations of ocean waves traveling into sea ice. *Journal of Geophysical Research*, *107*(C8), 3106. <https://doi.org/10.1029/2001JC000837>
- Squire, V. (2007). Of ocean waves and sea-ice revisited. *Cold Regions Science and Technology*, *49*(2), 110–133. <https://doi.org/10.1016/j.coldregions.2007.04.007>
- Squire, V. A., Dugan, J. P., Wadhams, P., Rottier, P. J., & Liu, A. K. (1995). Of ocean waves and sea ice. *Annual Review of Fluid Mechanics*, *27*(1), 115–168. <https://doi.org/10.1146/annurev.fl.27.010195000555>
- Squire, V. A., & Moore, S. C. (1980). Direct measurement of the attenuation of ocean waves by pack ice. *Nature*, *283*, 365–368. <https://doi.org/10.1038/283365a0>
- Steele, M. (1992). Sea ice melting and floe geometry in a simple ice-ocean model. *Journal of Geophysical Research*, *97*, 17729–17738. <https://doi.org/10.1029/92JC01755>
- Stroeve, J., Hamilton, L. C., Bitz, C. M., & Blanchard-Wrigglesworth, E. (2014). Predicting september sea ice: Ensemble skill of the search sea ice outlook 2008–2013. *Geophysical Research Letters*, *41*, 2411–2418. <https://doi.org/10.1002/2014GL059388>
- Stroeve, J. C., Serreze, M. C., Holland, M. M., Kay, J. E., Malanik, J., & Barrett, A. P. (2011). The arctic’s rapidly shrinking sea ice cover: A research synthesis. *Climatic Change*, *110*(3), 1005–1027. <https://doi.org/10.1007/s10584-011-0101-1>
- Sutherland, G., & Rabault, J. (2016). Observations of wave dispersion and attenuation in landfast ice. *Journal of Geophysical Research: Oceans*, *121*, 1984–1997. <https://doi.org/10.1002/2015JC011446>
- Sutherland, P., & Gascard, J.-C. (2016). Airborne remote sensing of ocean wave directional wavenumber spectra in the marginal ice zone. *Geophysical Research Letters*, *43*, 5151–5159. <https://doi.org/10.1002/2016GL067713>

- Sutherland, P., & Melville, W. K. (2015). Field measurements of surface and near-surface turbulence in the presence of breaking waves. *Journal of Physical Oceanography*, *45*(4), 943–965.
- The WAVEWATCH III[®] Development Group (WW3DG) (2016). *User manual and system documentation of WAVEWATCH III[®] version 5.16* (NOAA/NWS/NCEP/MMAB Tech. Note 329, 326 pp. + Appendices). College Park, MD.
- Thomson, J. (2012). Wave breaking dissipation observed with SWIFT drifters. *Journal of Atmospheric and Oceanic Technology*, *29*, 1866–1882. <https://doi.org/10.1175/JTECH-D-12-00018.1>
- Thomson, J., & Rogers, W. E. (2014). Swell and sea in the emerging arctic ocean. *Geophysical Research Letters*, *41*, 3136–3140. <https://doi.org/10.1002/2014GL059983>
- Thomson, J., Ackley, S., Girard-Arduin, F., Arduin, F., Babanin, A., Boutin, G., et al. (2018). Overview of the Arctic sea state and boundary layer physics program. *Journal of Geophysical Research*, *123*. <https://doi.org/10.1002/2018JC013766>
- Tolman, H. L. (1991). A Third-generation model for wind-waves on slowly varying, unsteady, and inhomogeneous depths and currents. *Journal of Physical Oceanography*, *21*(6), 782–797.
- Wadhams, P. (1973). Attenuation of swell by sea ice. *Journal of Geophysical Research*, *78*, 3552–3563. <https://doi.org/10.1029/JC078i018p03552>
- Wadhams, P. (1975). Airborne laser profiling of swell in an open ice field. *Journal of Geophysical Research*, *80*, 4520–4528. <https://doi.org/10.1029/JC080i033p04520>
- Wadhams, P., Lange, M. A., & Ackley, S. F. (1987). The ice thickness distribution across the atlantic sector of the antarctic ocean in midwinter. *Journal of Geophysical Research: Oceans*, *92*, 14535–14552. <https://doi.org/10.1029/JC092iC13p14535>
- Wadhams, P., Squire, V. A., Ewing, J. A., & Pascal, R. W. (1986). The effect of the marginal ice zone on the directional wave spectrum of the ocean. *Journal of Physical Oceanography*, *16*, 358–376.
- Wadhams, P., Squire, V. A., Goodman, D. J., Cowan, A. M., & Moore, S. C. (1988). The attenuation rates of ocean waves in the marginal ice zone. *Journal of Geophysical Research*, *93*, 6799–6818. <https://doi.org/10.1029/JC093iC06p06799>
- Walsh, E. J., D. W. H. III, Hines, D. E., Swift, R. N., & Scott, J. F. (1985). Directional wave spectra measured with the surface contour radar. *Journal of Physical Oceanography*, *15*, 566–592.
- Weber, J. E. (1987). Wave drift and wave attenuation in the marginal ice zone. *Journal of Physical Oceanography*, *17*, 2352–2361.
- Young, I. R., Rosenthal, W., & Ziemer, F. (1985). A three-dimensional analysis of marine radar images for the determination of ocean wave directionality and surface currents. *Journal of Geophysical Research: Oceans*, *90*, 1049–1059. <https://doi.org/10.1029/JC090iC01p01049>